Journal of Computational Physics 556 (2026) 114804

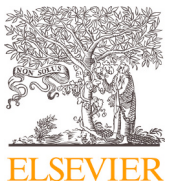

Contents lists available at ScienceDirect

Journal of Computational Physics

journal homepage: www.elsevier.com/locate/jcp

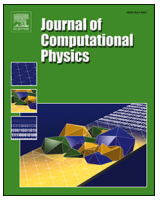

# A moving-least-squares reconstruction of the hydrodynamic loads on deformable bodies: Application to immersed boundary methods

Giovanni Vagnoli [a], Martino A. Scarpolini [a], Roberto Verzicco [a,b,c], Francesco Viola [a,*]

[a] Gran Sasso Science Institute (GSSI), Viale Luigi Rendina, 26, L'Aquila, 67100, Italy
[b] Tor Vergata University of Rome, Via del Politecnico 1, Rome, 00133, Italy
[c] Department of Physics, Mesa+ Institute, and J. M. Burgers Centre for Fluid Dynamics, University of Twente, AE Enschede, Twente, 7500, The Netherlands

ARTICLE INFO

*Keywords:*
Fluid-structure interaction
Hydrodynamic stresses
Immersed boundary method

ABSTRACT

Immersed boundary methods (IBMs) provide a convenient and efficient approach for fluid-structure interaction (FSI) problems, as they allow for flexible handling of moving boundaries without conforming mesh requirements. However, computing the hydrodynamic loads exerted by the fluid on the immersed body is a well-known issue, as fluid grid points are not directly available on the wet surface. In the literature, several procedures have been proposed, but they typically yield non-smooth stress distributions or have low accuracy. On the other hand, higher-order methods can only be applied to rigid bodies in the limit of boundary layer flow. In this paper, we propose a novel procedure capable of accurately evaluating the stresses acting on solid surfaces, which is based on a truncated Taylor series of the whole fluid stress tensor, without relying on any assumption on the underlying flow or body dynamics. The terms of the Taylor series are evaluated directly from the flow solution using a versatile moving-least-squares (MLS) interpolation with a small computational overhead. We also propose a variation of the procedure for computing hydrodynamic loads within thin lubrication layers, which can arise during the interaction of multiple deformable bodies mediated by a fluid. The method is validated in a series of numerical experiments encompassing analytical flow solutions, separated flows over rigid bodies, and FSI over rigid and deformable bodies. Although the method is here applied to a second-order IBM code, it can be applied to any-order fluid solver, including body-fitted ones.

## 1. Introduction

Fluid-structure interaction (FSI) is key in many scientific applications. The dynamic interplay between fluid and moving walls can be found in various engineering applications, such as the vibration of structures induced by the presence of vortices [1–3], but also in biological frameworks, such as insect flight [4] or the haemodynamics within the human heart [5,6]. In these cases, the motion of the surrounding fluid produces local stresses over the wet surface which, along with internal elastic stresses, causes the deformation and displacement of the body. In turn, the moving/deforming body surface affects the flow evolution through the no-slip boundary condition. This non-linear coupling can lead to complex structure dynamics and the corresponding FSI has to be solved numerically [7,8].

* Corresponding author.
*E-mail addresses:* giovanni.vagnoli@gssi.it (G. Vagnoli), martino.scarpolini@gssi.it (M.A. Scarpolini), roberto.verzicco@gssi.it (R. Verzicco), francesco.viola@gssi.it (F. Viola).

https://doi.org/10.1016/j.jcp.2026.114804
Received 27 June 2025; Accepted 21 February 2026
Available online 26 February 2026

In this framework, body-fitted approaches, such as the Finite Volumes or Finite Elements methods, can suffer significant computational overhead with respect to fixed-boundary-flows as they require to continuously update the fluid mesh according to the instantaneous body configuration and the flow solution should be interpolated to the updated grid [9,10]. This issue is alleviated by immersed boundary methods (IBMs), where the fluid grid has not to be conformal to the body surface and the FSI coupling is obtained by updating the immersed boundary (IB) forcing which depends on the instantaneous body position and on the flow solution [11–14]. Furthermore, IBMs are typically based on fractional-step methods exploiting low order spatial discretisation over Cartesian meshes, which allow for the use of highly efficient solvers entailing the inversion of reduced-band matrices and fast trigonometric expansions for the elliptic equation [15,16].

However, the advantage of a fixed fluid mesh comes at the cost of not having boundary of the body coinciding with a coordinate surface, thus making challenging the evaluation of the stresses exerted by the fluid on the walls. This is a well-known issue of IBMs and several approaches have been proposed to make up for this problem. In particular, smooth hydrodynamic forces can be computed directly from the IB forcing using the Newton third law of motion [11]. Despite being efficient, this approach can be applied only to rigid bodies enclosing a finite volume and cannot distinguish between viscous and pressure loads. To avoid these drawbacks, the stress tensor can be reconstructed directly from the underlying flow by interpolating pressure and velocity fields in a point near the wall (referred to as probe) and transferring the stress tensor to the wall [12,17]. In order to improve the first order accuracy of this method, the tangent-to-the-wall velocity and pressure has been reconstructed near the surface using polynomial wall functions whose free-parameters are determined *online* during the simulation [18]. This effective approach has been applied to solve turbulence/particle interactions [18], FSI with fracturing [19] and the dynamics of melting/moving bodies [20]. More recently, this method has been revised by using different strategies to evaluate the coefficients of the reconstruction polynomials [21]. Although this polynomial reconstruction approach allows to achieve a higher order of accuracy, it is conceived for rigid bodies under the boundary layer assumption, and cannot be applied to deformable bodies, undergoing either imposed kinematics or FSI. Recently, higher order evaluation of the hydrodynamic loads has been achieved employing a two-probes approach [22].

To fill this gap, in this work a novel procedure capable of accurately evaluating the stresses acting on solid surfaces is proposed. The method is based on a truncated Taylor series of the whole fluid stress tensor without relying on any assumption on the underlying flow or body dynamics. The terms of the Taylor series are evaluated directly from the flow solution using a versatile moving-least-squares (MLS) interpolation, already widely used in the IBM community to build the IB forcing [12,17]. The proposed methodology can be easily employed to obtain high order hydrodynamic loads and, although it is here embedded in a second-order fluid solver based on IBM, it can be applied to any-order fluid solver, including body-fitted ones. The resulting procedure is cost efficient and it can be applied to any rigid or deformable body. The method is validated in a series of numerical experiments encompassing analytical flow solutions, fixed wet bodies and FSI over rigid and deformable bodies.

The paper is organised as follows: in Section 2, the standard FSI framework using the IB direct forcing method in the MLS fashion is introduced. Moreover, the methods from the literature that are used to evaluate the stresses are briefly reviewed; in Section 3, we introduce our novel method, showing two alternative approaches, one of them tailored to solve the hydrodynamic loads within lubrication layers between solid bodies; in Section 4, the method is firstly applied to analytical flows to test its order of accuracy, then to two-dimensional (2D) and three-dimensional (3D) test cases solved numerically; finally, the conclusions are presented in Section 5.

## 2. Problem formulation and numerical method

### 2.1. Governing equations

Let consider the motion of the body $\Omega$ depicted in Fig. 1 within an incompressible fluid of density $\rho$ and dynamic viscosity $\mu$. The fluid motion is governed by the incompressible Navier-Stokes equations, which in nondimensional form read:

$$\frac{\partial \mathbf{u}}{\partial t} + \nabla \cdot (\mathbf{u} \otimes \mathbf{u}) = -\nabla p + \frac{1}{Re}\nabla^2 \mathbf{u} + \mathbf{f}, \tag{1a}$$

$$\nabla \cdot \mathbf{u} = 0, \tag{1b}$$

where $\mathbf{u}$ and $p$ are the flow velocity and pressure. $Re = \rho U L/\mu$ is the Reynolds number based on a characteristic length $L$ and velocity $U$. The no-slip boundary condition $\mathbf{u} = \mathbf{U}^b$ is imposed at the fluid/solid boundary through the IB forcing term $\mathbf{f}$. $\mathbf{U}^b$ is the local velocity of the body surface, given by the structural dynamics - either rigid or deformable - which depends on the traction $\mathbf{t}$ exerted by the surrounding fluid on the structure.

### 2.2. Numerical method

Although the focus of the paper is on the accurate evaluation of the hydrodynamic stress, which does not depend on the details of the discretization scheme and of the IB method used, we briefly outline the numerical algorithm employed in the numerical tests. In doing so, we also introduce the MLS interpolation framework, which is not only needed for evaluating the IB forcing, but also serves as a key component of the proposed method.

The fluid Eq. (1) are advanced in time using a fractional step method [15,23]. The momentum Eq. (1a) is advanced from time $t^n$ to $t^{n+1}$ using an implicit Crank-Nicholson scheme for the viscous term and an explicit Adam-Bashfort scheme for the non-linear term. The equations are discretised in space using a second-order accurate centred finite-difference (FD) scheme on a Cartesian staggered grid, hereafter denoted as Eulerian grid. $N_1$, $N_2$ and $N_3$ points are used in each direction, and the corresponding grid size in the three

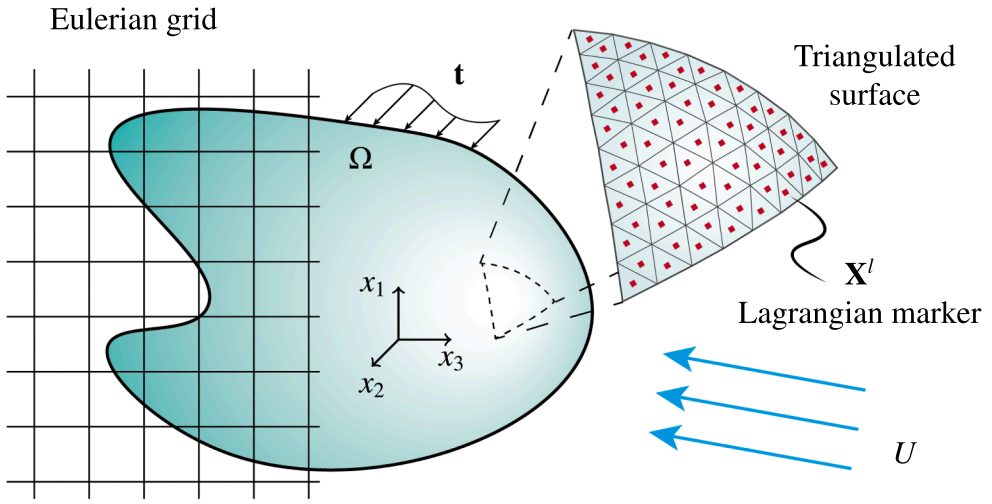


**Fig. 1.** Sketch of the numerical setting used for the FSI problems. The fluid domain is discretised by means of a structured Eulerian grid. The body surface is discretised using triangular elements, whose centroids are the Lagrangian markers.

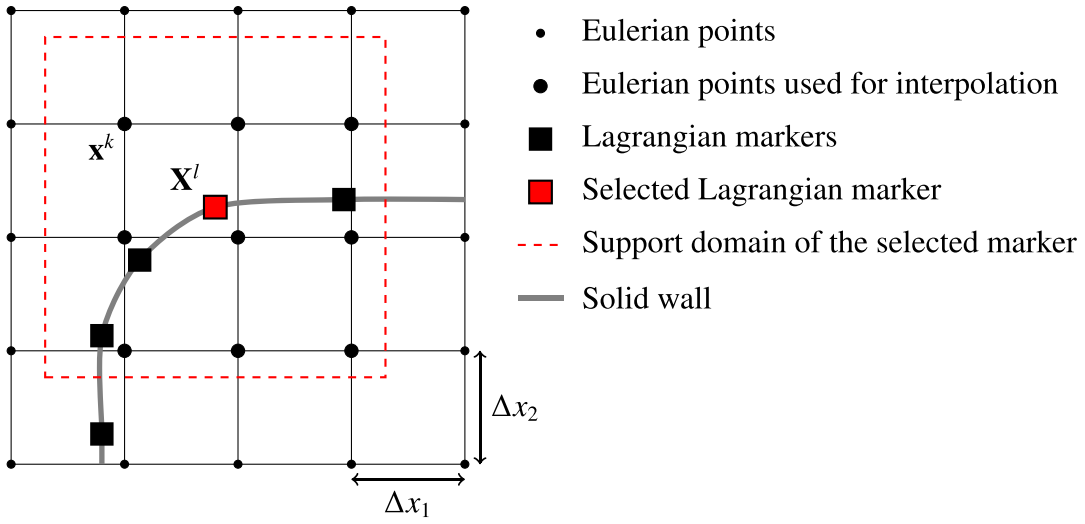


**Fig. 2.** 2D sketch of the setting required to perform the IB treatment. For the selected marker, the corresponding supporting domain used for the MLS interpolation is represented by a dashed line.

spatial directions of the $k$th Eulerian cell is $\Delta x_1^k$, $\Delta x_2^k$ and $\Delta x_3^k$. Periodic boundary conditions are applied in the $x_1$ and $x_2$ directions, while along $x_3$ Dirichlet or radiative conditions are enforced [24].

The IB forcing is applied to the provisional velocity $\hat{\mathbf{u}}$ to enforce the no-slip condition. Following the explicit direct forcing method [11], the surface of the body is discretized by $N_t$ triangular elements, and at their centroids $\mathbf{X}^l$, $l = 1, \dots, N_t$, are collocated the Lagrangian markers (see Fig. 1). The position and velocity of the markers are assumed to be known at each time step from the solution of the structural dynamics. The IB forcing $\mathbf{F}$ on the $l$th Lagrangian marker is thus evaluated as follows:

$$\mathbf{F}(\mathbf{X}^l) = \frac{\mathbf{U}^b(\mathbf{X}^l) - \hat{\mathbf{U}}(\mathbf{X}^l)}{\Delta t^n}, \tag{2}$$

where $\Delta t^n = t^{n+1} - t^n$ and $\hat{\mathbf{U}}(\mathbf{X}^l)$ is the interpolation of $\hat{\mathbf{u}}$ from the Eulerian grid to the Lagrangian marker $\mathbf{X}^l$. The interpolation operator is built using MLS kernels [12,17,25]. For each velocity component $i$, a support domain containing $N_E$ Eulerian points $\mathbf{x}^k$ is created, centred at the marker $\mathbf{X}^l$. Typically, $N_E = 27$ in three- and $N_E = 9$ in two-dimensions (see Fig. 2).

The interpolation rule is given by:

$$\hat{U}_i(\mathbf{X}^l) = \sum_{k=1}^{N_E} \phi_k(\mathbf{X}^l)\hat{u}_i(\mathbf{x}^k), \tag{3}$$

where the basis functions $\phi_k(\mathbf{X}^l)$ are obtained as detailed in Appendix A. Lastly, the force is distributed to the underlying Eulerian grid exploiting again the MLS basis functions:

$$f_i(\mathbf{x}^k) = \sum_{l=1}^{N_t} c_l\, \phi_k(\mathbf{X}^l)\, F_i(\mathbf{X}^l), \tag{4}$$

where the coefficient $c_l = \Delta V_l / \sum_{k=1}^{N_E} \phi_k(\mathbf{X}^l)\Delta v^k$ assures that momentum is conserved during the force spreading [12]. The volume associated to the Lagrangian markers is $\Delta V_l = A_l \sum_{k=1}^{N_E} \phi_k(\mathbf{X}^l)\left(\Delta x_1^k + \Delta x_2^k + \Delta x_3^k\right)/3$, with $A_l$ the area of the $l$th triangle, and $\Delta v^k = \Delta x_1^k\, \Delta x_2^k\, \Delta x_3^k$ is the volume of the $k$th Eulerian cell.

To satisfy Eq. (1b), the velocity field just calculated (and satisfying no-slip condition) is projected onto a divergence-free space by means of the pseudopressure $\varphi$, which is calculated upon the solution of a Poisson equation using fast Fourier transforms in the periodic directions [15]. Finally, the pressure is updated using $\varphi$.

### 2.3. Hydrodynamics loads computation

In the case of FSI, a fundamental step for the resolution of the coupled problem is the evaluation of the local hydrodynamic stress over the wet surfaces, which serves as input for the structural solver. Nevertheless, even if the body is fixed or its kinematic is prescribed, it is relevant for several applications to measure the hydrodynamic loads exerting on the solid bodies. For an incompressible flow, the fluid stress tensor $T$ depends on the velocity and pressure fields as follows:

$$T = -p\, I + \frac{1}{Re}\left[\nabla\mathbf{u} + \nabla\mathbf{u}^T\right], \tag{5}$$

being $I$ the identity matrix and $[\nabla\mathbf{u}]_{ij} = \partial u_j/\partial x_i$ the velocity gradient tensor. The traction $\mathbf{t}$ acting on the marker $\mathbf{X}^l$ of the surface with normal $\mathbf{n}^l$ is given by:

$$\mathbf{t}(\mathbf{X}^l) = T(\mathbf{X}^l)\cdot\mathbf{n}^l = -p(\mathbf{X}^l)\,\mathbf{n}^l + \frac{1}{Re}\left[\nabla\mathbf{u}(\mathbf{X}^l) + \nabla\mathbf{u}^T(\mathbf{X}^l)\right]\cdot\mathbf{n}^l, \tag{6}$$

where $p(\mathbf{X}^l)$ and $\nabla\mathbf{u}(\mathbf{X}^l)$ are the pressure and velocity gradient evaluated on $\mathbf{X}^l$. The resultant hydrodynamic force $\mathbf{R}$ and torque $\mathbf{M}^O$ with respect to the pole $\mathbf{x}^O$ acting on the body can be evaluated as follows:

$$\mathbf{R} = \sum_{l=1}^{N_t} \mathbf{t}(\mathbf{X}^l)\, A_l, \quad \mathbf{M}^O = \sum_{l=1}^{N_t} \mathbf{r}_l^O \times \mathbf{t}(\mathbf{X}^l)\, A_l, \tag{7}$$

with $\mathbf{r}_l^O = \mathbf{X}^l - \mathbf{x}^O$. If the body considered is wet on both sides, then a positive $\mathbf{n}_+^l$ and a negative $\mathbf{n}_-^l = -\mathbf{n}_+^l$ normal vectors can be defined and the traction acting on the $l$th marker is given by:

$$\mathbf{t}(\mathbf{X}^l) = \mathbf{t}_+(\mathbf{X}^l) - \mathbf{t}_-(\mathbf{X}^l), \tag{8}$$

being $\mathbf{t}_+$ and $\mathbf{t}_-$ the hydrodynamic tractions evaluated using $\mathbf{n}_+^l$ and $\mathbf{n}_-^l$, respectively.

However, since the Eulerian grid - where the Navier-Stokes equations are solved - is not body conformal, the pressure and velocity gradients obtained from the fluid solver are not defined on the Lagrangian marker $\mathbf{X}^l$. This issue has been circumvented in [12,17], by considering a probe point cast for each marker in the wall normal direction:

$$\mathbf{X}^P = \mathbf{X}^l + h\,\mathbf{n}^l, \tag{9}$$

being $h$ the length of the probe, which should be sufficiently long to avoid contamination of the results by the flow solution on the opposite wet side of the boundary (see next Section for further details). To satisfy this condition for any orientation of the wet surface with respect to the Eulerian grid, the probe length should be $h = 1.5\Delta_d$, being $\Delta_d$ the length of the diagonal of the closest Eulerian cell to the marker. For instance, for a uniform grid with spacing $\Delta$, the probe length should be $h = 1.5\sqrt{3}\,\Delta$ in 3D cases and $h = 1.5\sqrt{2}\,\Delta$ in 2D problems. The velocity gradient field is transferred back to the marker as $\nabla\mathbf{u}|_{\mathbf{X}^l} = \nabla\mathbf{u}|_{\mathbf{X}^P} + \mathcal{O}(h)$. On the contrary, the pressure field is expanded in Taylor series at first order from the Lagrangian marker to the probe point $p(\mathbf{X}^l) = p(\mathbf{X}^P) - \partial p/\partial n|_{\mathbf{X}^l} h + \mathcal{O}(h^2)$. To estimate the value of $\partial p/\partial n|_{\mathbf{X}^l}$, the normal-to-the-wall component of Eq. (1a) is written at point $\mathbf{X}^l$, obtaining $\mathrm{d}U_n^b(\mathbf{X}^l)/\mathrm{d}t = -\partial p/\partial n|_{\mathbf{X}^l} + Re^{-1}\nabla^2 u_n|_{\mathbf{X}^l}$, being $U_n^b$ and $u_n$ the normal component of the body and fluid velocity. The IB forcing in the MLS fashion reconstruct a linear velocity field near the boundary [12,26], thus $\nabla^2 u_n|_{\mathbf{X}^l} = 0$, yielding the following approximate expression for the normal pressure derivative:

$$\left.\frac{\partial p}{\partial n}\right|_{\mathbf{X}^l} \simeq -\frac{\mathrm{d}U_n^b(\mathbf{X}^l)}{\mathrm{d}t}. \tag{10}$$

Despite this method entails a low computational overhead and allows to deal with solid and deformable bodies, it can reach at most a first order accuracy for the viscous stress, while the second order accuracy for the pressure loads can be achieved only under restrictive hypothesis on the shape of the flow near the wall.

Higher order accuracy can be obtained using a field reconstruction method near the solid wall [18]. Using the boundary layer hypothesis, pressure and tangent-to-the-wall velocity component $u_\tau$ are expressed as polynomials in the normal direction $n$, going from the marker $\mathbf{X}^l$ (corresponding to $n = 0$) to the probe point $\mathbf{X}^P$ ($n = h$):

$$p(n) = c_p + b_p\, n + \frac{1}{2}a_p\, n^2, \quad u_\tau(n) = d_u + c_u\, n + \frac{1}{2}b_u\, n^2 + \frac{1}{6}a_u\, n^3, \tag{11}$$

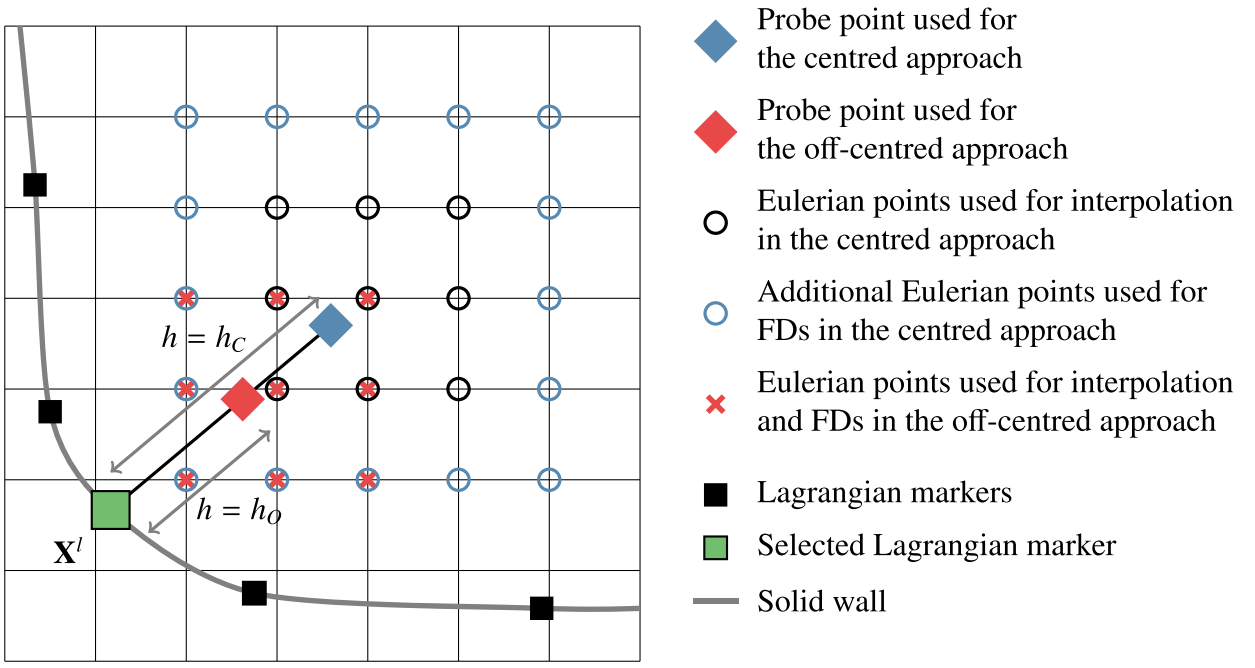


**Fig. 3.** 2D sketch of the probe position and its support domain to evaluate the stress tensor at point $\mathbf{X}^l$. The Eulerian points involved in the FDs and interpolation are highlighted for the centred and off-centred scheme together with the corresponding probe position and length of the probe $h_C$ and $h_O$. All points used to compute derivatives and MLS interpolation must lie on the same wet side.

being $\{a_p, b_p, c_p\}$ and $\{a_u, b_u, c_u, d_u\}$ sets of unknown coefficients to be determined. Three conditions are thus needed to fit the pressure polynomial: in addition to the one introduced above (Eq. (10) at $n = 0$), the values of $p$ and $\partial p/\partial n$ at the probe ($n = h$) are set equal to the values coming from the numerical flow solution. Alternatively, the first condition can be dropped by imposing the second $n$-derivative of pressure in $n = h$ [21]. Concerning the velocity $u_\tau$, three conditions are obtained by imposing the value of the tangential velocity and of its first and second derivative in the normal direction at the probe location. The last condition, instead, is obtained using the boundary layer equations over the flat plate, yielding $\partial^3 u_\tau/\partial n^3|_{\mathbf{X}^P} \simeq Re \sum_{q,r=1}^{3} \partial^2 p/\partial x_q \partial x_r n_q^l n_r^l$ at the probe point, being $n_q^l, n_r^l$ the $q$ and $r$ components of the normal vector $\mathbf{n}^l$ [18], or imposing the tangential wall velocity, i.e. $u_\tau = U_\tau^b$ [21]. In this way, the stress component $Re^{-1}\partial u_\tau/\partial n$ is evaluated from the analytical derivative of the polynomial at $n = 0$.

The above mentioned procedure is the base of most of boundary reconstruction methods in the context of IBMs. A possible weakness is that the terms $\partial u_n/\partial n$ and $\partial u_n/\partial \tau$ are completely disregarded, making the implicit assumption that they are negligible. In fact, the former is usually small compared to pressure, while the latter is exactly zero although this is true only for rigid bodies. In contrast, in the case of a deformable body $\partial u_n/\partial \tau$ is the gradient of the deformation velocity at the wall, which in general is not null. Moreover, the pressure condition at the wall (Eq. (10)) does not always hold true, especially in curved and/or deforming bodies.

## 3. A MLS based method to evaluate the whole stress tensor at the wall

In this section, we propose an improved methodology to evaluate the hydrodynamic loads at the wall, regardless of the rigid or deformable nature of the structure. The method is based on a truncated Taylor expansion of the whole stress tensor in the near wall region, which is evaluated using MLS kernels. Although the method is presented in the framework of a second order MLS-IB method, it can be applied to any CFD solver matching the accuracy of the underlying numerical scheme.

### 3.1. Truncated Taylor series of the stress tensor components

Following the sketch of Fig. 3, given a Lagrangian marker $\mathbf{X}^l$ on the body surface, the corresponding normal probe point is built using Eq. (9). Then, assuming the flow field is sufficiently differentiable, we can consider the following truncated Taylor-series expansion of the pressure and velocity gradients, from the probe point $\mathbf{X}^P$ backwards to the wall location $\mathbf{X}^l$:

$$p(\mathbf{X}^l) = p(\mathbf{X}^P) - \left.\frac{\partial p}{\partial n}\right|_{\mathbf{X}^P} h + \frac{1}{2}\left.\frac{\partial^2 p}{\partial n^2}\right|_{\mathbf{X}^P} h^2 + \mathcal{O}(h^3), \tag{12a}$$

$$\left.\frac{\partial u_i}{\partial x_j}\right|_{\mathbf{X}^l} = \left.\frac{\partial u_i}{\partial x_j}\right|_{\mathbf{X}^P} - \left.\frac{\partial}{\partial n}\left(\frac{\partial u_i}{\partial x_j}\right)\right|_{\mathbf{X}^P} h + \frac{1}{2}\left.\frac{\partial^2}{\partial n^2}\left(\frac{\partial u_i}{\partial x_j}\right)\right|_{\mathbf{X}^P} h^2 + \mathcal{O}(h^3), \tag{12b}$$

where the normal derivatives are defined as $\partial/\partial n|_{\mathbf{X}^P} = \sum_{q=1}^{3} n_q^l\, \partial/\partial x_q$ and $\partial^2/\partial n^2|_{\mathbf{X}^P} = \sum_{q,r=1}^{3} n_q^l n_r^l\, \partial^2/\partial x_q \partial x_r$.

In general, the probe point does not coincide with an Eulerian grid point (it cannot for any Cartesian direction if a staggered grid is employed), and the coefficients of the Taylor series involving the pressure and velocity derivatives have to be computed from the flow solution through interpolation.

### 3.2. Evaluation of the Taylor series coefficients by a centred FD approach

To evaluate the coefficients of Eq. (12a), we can interpolate the pressure from the Eulerian grid to the probe point $\mathbf{X}^P$ using the same MLS kernels adopted for the IB forcing (Section 2). For each $\mathbf{X}^P$, a supporting domain of interpolation of $N_E = 27$ Eulerian grid points in 3D and $N_E = 9$ points in 2D (Fig. 3) is built, and the MLS kernels $\phi_k(\mathbf{X}^P)$ are constructed as detailed in Appendix A. The $\phi_k(\mathbf{X}^P)$ are then used to interpolate the flow quantities from the Eulerian grid to the probe point $\mathbf{X}^P$ using the same expression as Eq. (3). Thus, the first term of Eq. (12a) is given by:

$$p(\mathbf{X}^P) = \sum_{k=1}^{N_E} \phi_k(\mathbf{X}^P) p(\mathbf{x}^k), \tag{13}$$

where $p(\mathbf{x}^k)$ is the pressure evaluated at the Eulerian grid points $\mathbf{x}^k$, which is directly computed by the fluid solver. The higher order terms of the expansion can be evaluated using the same basis functions:

$$\left.\frac{\partial p}{\partial n}\right|_{\mathbf{X}^P} = \sum_{q=1}^{3} n_q^l \sum_{k=1}^{N_E} \phi_k(\mathbf{X}^P) \left.\frac{\partial p}{\partial x_q}\right|_{\mathbf{x}^k}, \quad \left.\frac{\partial^2 p}{\partial n^2}\right|_{\mathbf{x}^k} = \sum_{q,r=1}^{3} n_q^l n_r^l \sum_{k=1}^{N_E} \phi_k(\mathbf{X}^P) \left.\frac{\partial^2 p}{\partial x_q \partial x_r}\right|_{\mathbf{x}^k}. \tag{14}$$

In order to keep the convergence rate of the MLS interpolation and of the underlying numerical scheme, the derivatives on the Eulerian grid points $\partial p/\partial x_q|_{\mathbf{x}^k}$ and $\partial^2 p/\partial x_q \partial x_r|_{\mathbf{x}^k}$ are evaluated by a second order centred FD scheme, as detailed in Appendix B. We anticipate that the use of the centred FD scheme for the evaluation of the derivatives on the points $\mathbf{x}^k$ requires a probe length equal to $2.5\Delta_d$, as discussed in detail below. Therefore, all the terms of the Taylor series are calculated with a second order of accuracy, leading to an estimation of $p(\mathbf{X}^l)$ that is $\mathcal{O}(\Delta_d^2)$.

The same procedure outlined above can be used to determine the coefficients of Eq. (12b), interpolating the velocity gradient from the Eulerian grid to the probe point via the MLS kernels. Therefore, the first two coefficients of Eq. (12b) are given by:

$$\left.\frac{\partial u_i}{\partial x_j}\right|_{\mathbf{X}^P} = \sum_{k=1}^{N_E} \phi_k(\mathbf{X}^P) \left.\frac{\partial u_i}{\partial x_j}\right|_{\mathbf{x}^k} \quad \left.\frac{\partial}{\partial n}\left(\frac{\partial u_i}{\partial x_j}\right)\right|_{\mathbf{X}^P} = \sum_{q=1}^{3} n_q^l \sum_{k=1}^{N_E} \phi_k(\mathbf{X}^P) \left.\frac{\partial^2 u_i}{\partial x_j \partial x_q}\right|_{\mathbf{x}^k}, \tag{15}$$

where the derivatives $\partial u_i/\partial x_j|_{\mathbf{x}^k}$ and $\partial^2 u_i/\partial x_j \partial x_q|_{\mathbf{x}^k}$ are defined on the Eulerian points and can be evaluated from the flow solution. The direct calculation of the last coefficient of Eq. (12b), involving the third derivatives of the velocity field, through FD would entail to further enlarge the stencil. This issue can be circumvented by exploiting the derivatives of the MLS interpolation kernels:

$$\left.\frac{\partial^2}{\partial n^2}\left(\frac{\partial u_i}{\partial x_j}\right)\right|_{\mathbf{X}^P} = \sum_{q,r=1}^{3} n_q^l n_r^l \sum_{k=1}^{N_E} \left.\frac{\partial \phi_k}{\partial x_r}\right|_{\mathbf{X}^P} \left.\frac{\partial^2 u_i}{\partial x_j \partial x_q}\right|_{\mathbf{x}^k}, \tag{16}$$

where $\partial\phi_k/\partial x_r$ is the derivative of the MLS basis functions [25] (see Appendix A). Eq. (16) provides an effective first order evaluation of the last Taylor coefficient, which is then multiplied by $h^2$ thus preserving the overall accuracy of the method.

It should be noted that, computing all flow derivatives on the MLS support domain through centred FD entails an increase of the effective number of Eulerian points involved in the evaluations of the stresses with respect to the $N_E$ points required for the MLS interpolation. Indeed, following the sketch of Fig. 3, to evaluate the Eulerian derivatives on the points within the supporting domain of interpolation of $\mathbf{X}^P$, additional layers of points must be considered in each spatial direction, thus enlarging the effective supporting domain for the evaluation of the traction from 3 to $3+2$ points per direction. Therefore, instead of the typical 27 Eulerian points required for the MLS interpolation, the supporting domain for the evaluation of the stresses is enlarged to 125 points. Since all such points must lie on the same side of the IB to avoid contamination in the calculation of the derivatives and in the subsequent MLS interpolation, the probe must be sufficiently long. Given a body having a generic orientation with respect to the Eulerian grid, the probe length to ensure that all derivatives/interpolation points are located on the same wet side of the wall is $h_C = 2.5\,\Delta_d$. For instance, employing a uniform grid with spacing $\Delta$ would lead to a probe with length $h_C = 2.5\sqrt{3}\,\Delta \simeq 4.33\Delta$ in 3D and $h_C = 2.5\sqrt{2}\,\Delta \simeq 3.54\Delta$ in 2D. Although this probe (longer than the one typically employed in IBM-MLS, see Section 2) can be seamlessly used in many flow cases, it may become a limitation when stresses need to be measured in thin lubrication layers. Therefore, we propose a variation of the method tailored for evaluating the stresses using a shorter probe.

### 3.3. Evaluation of the Taylor series coefficients with an off-centred FD approach

Instead of using a centred FD approximation for the coefficient of the Taylor series, an off-centred FD scheme is employed here, using only the same $N_E$ Eulerian points required for the MLS interpolation. In particular, for each point in which the derivatives are evaluated, the FD stencil is dynamically updated to be composed of a subset of the Eulerian points within the MLS supporting domain of interpolation. The details of the off-centred stencils and the relative FD approximations employed in this work can be found in Appendix B. In this way, the probe length reduces to $h_O = 1.5\Delta_d$ (see Fig. 3), i.e. it is the same as then one typically employed in IBM-MLS. Furthermore, having a probe closer to the wall, the precision of the expansions (12a) is expected to increase. Following this

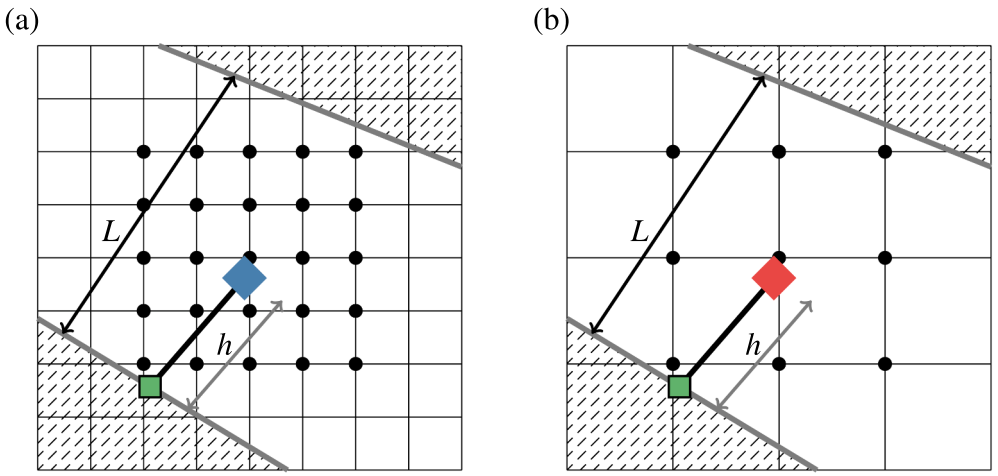


**Fig. 4.** 2D sketch of a contact problem involving two planar surfaces approaching each other. Detail of the minimal grid size required to correctly evaluate the stresses at the wall up to the cut-off length $L$ with (a) the centred and (b) the off-centred approach. The black dots highlight the Eulerian points involved in the evaluation of the Eulerian derivatives in Eq. (12).

**Table 1**
Summary of the various series expansion considered in Section 4.

| | Abbreviation | Expansion considered |
|---|---|---|
| Pressure | Order 1 | $p(\mathbf{X}^I) = p(\mathbf{X}^P)$ |
| | Order 2 | $p(\mathbf{X}^I) = p(\mathbf{X}^P) - \frac{\partial p}{\partial n}\Big\vert_{\mathbf{X}^P} h$ |
| | Order 2$^+$ | $p(\mathbf{X}^I) = p(\mathbf{X}^P) - \frac{\partial p}{\partial n}\Big\vert_{\mathbf{X}^P} h + \frac{1}{2}\frac{\partial^2 p}{\partial n^2}\Big\vert_{\mathbf{X}^P} h^2$ |
| Velocity gradient | Order 1 | $\frac{\partial u_i}{\partial x_j}\Big\vert_{\mathbf{X}^I} = \frac{\partial u_i}{\partial x_j}\Big\vert_{\mathbf{X}^P}$ |
| | Order 2 | $\frac{\partial u_i}{\partial x_j}\Big\vert_{\mathbf{X}^I} = \frac{\partial u_i}{\partial x_j}\Big\vert_{\mathbf{X}^P} - \frac{\partial}{\partial n}\left(\frac{\partial u_i}{\partial x_j}\right)\Big\vert_{\mathbf{X}^P} h$ |
| | Order 2$^+$ | $\frac{\partial u_i}{\partial x_j}\Big\vert_{\mathbf{X}^I} = \frac{\partial u_i}{\partial x_j}\Big\vert_{\mathbf{X}^P} - \frac{\partial}{\partial n}\left(\frac{\partial u_i}{\partial x_j}\right)\Big\vert_{\mathbf{X}^P} h + \frac{1}{2}\frac{\partial^2}{\partial n^2}\left(\frac{\partial u_i}{\partial x_j}\right)\Big\vert_{\mathbf{X}^P} h^2$ |

approach, the first derivative $\partial p/\partial x_q|_{\mathbf{x}^k}$ is evaluated with a second order of accuracy, using three stencil points per spatial direction. On the contrary, the second derivative $\partial^2 p/\partial x_q \partial x_r|_{\mathbf{x}^k}$ can be evaluated at most with a first order accuracy. Nevertheless, since this term is multiplied by $h^2 = \mathcal{O}(\Delta_d^2)$ in Eq. (12a), the estimation of $p(\mathbf{X}^I)$ is still second order accurate.

Analogously, the evaluation of the velocity first and second derivatives $\partial u_i/\partial x_j|_{\mathbf{x}^k}$, $\partial^2 u_i/\partial x_j \partial x_q|_{\mathbf{x}^k}$ on the Eulerian grid can be performed using an off-centred FD scheme. Instead, since only three stencil points are available in this framework, the third derivative of the velocity cannot be evaluated, and the highest order term in Eq. (12b) has to be neglected. Anyway, this method still preserves the second order of accuracy, since $\partial u_i/\partial x_j|_{\mathbf{X}^P}$ is evaluated at second order and $\partial(\partial u_i/\partial x_j)/\partial n|_{\mathbf{X}^P}$, evaluated at first order with the off-centred scheme is then multiplied by $h = \mathcal{O}(\Delta_d)$.

One could wonder which one between the centred (using the longer probe $h_C = 2.5\Delta_d$) and the off-centred (based on a further truncated expansion and using the shorter probe $h_O = 1.5\Delta_d$) approaches is preferable. A comparison can be made by looking at the ratio between the corresponding leading truncation errors $e_C$ and $e_O$:

$$\frac{e_C}{e_O} = \frac{\frac{1}{6}\left|\frac{\partial^3}{\partial n^3}\left(\frac{\partial u_i}{\partial x_j}\right)\Big\vert_{\mathbf{X}^{P_C}}\right| h_C^3}{\frac{1}{3}\left|\frac{\partial^2}{\partial n^2}\left(\frac{\partial u_i}{\partial x_j}\right)\Big\vert_{\mathbf{X}^{P_O}}\right| h_O^2} = \frac{\left|\frac{\partial^3}{\partial n^3}\left(\frac{\partial u_i}{\partial x_j}\right)\Big\vert_{\mathbf{X}^{P_C}}\right|}{\left|\frac{\partial^2}{\partial n^2}\left(\frac{\partial u_i}{\partial x_j}\right)\Big\vert_{\mathbf{X}^{P_O}}\right|} \frac{125}{36}\Delta_d, \tag{17}$$

where $\mathbf{X}^{P_C}$, $\mathbf{X}^{P_O}$ are the corresponding probe point for the two cases. Typically, the velocity field $u_i$ in the neighbouring of the solid wall is regular enough to assure that $\left|\partial^3(\partial u_i/\partial x_j)/\partial n^3|_{\mathbf{X}^{P_C}}\right| \Big/ \left|\partial^2(\partial u_i/\partial x_j)/\partial n^2|_{\mathbf{X}^{P_O}}\right| = \mathcal{O}(1)$, thus it results that the error ratio scales as $\Delta_d$. Hence, for an Eulerian grid sufficiently refined the centred approach is one order more accurate.

However, in the case of flows within thin lubrication layers, the off-centred scheme can be advantageous in terms of computational cost. Fig. 4 sketches a contact problem where two planar surfaces with a fluid in between are approaching while moving across a uniform Eulerian grid. Let suppose that the hydrodynamic forces should be computed until a certain (grid-independent) minimum distance in between the surfaces $L$ (as an example, $L$ may be a cut off length needed to activate a contact model). To assure that all the Eulerian points involved in the evaluation of the stresses fit within the thin layer of fluid, the length of the probe must satisfy $2h \leq L$, thus allowing a maximum grid size of $\Delta_C = L/5\sqrt{3}$ and $\Delta_O = L/3\sqrt{3}$ for the centred and off-centred schemes, respectively. Consequently, the ratio between the minimum number of grid points required to evaluate correctly the loads with the centred $N_C$

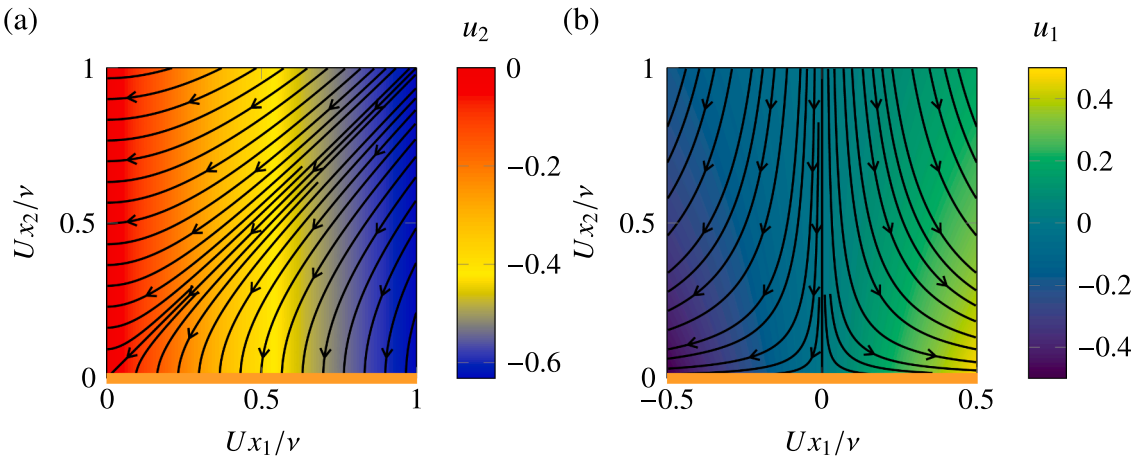


**Fig. 5.** (a) Contour plot of the $u_2$ component of the corner flow together with the flow streamlines. (b) Contour plot of the $u_1$ component of the stretching flow together with the flow streamlines. In both panels, the southern wall ($x_2 = 0$), where hydrodynamic stresses are evaluated, is highlighted by an orange line.

and off-centred $N_O$ scheme is $N_C = (5/3)^3 N_O \simeq 4.63\, N_O$. As an example, in cardiovascular flows, such as those involving contact phenomena during the opening and closing of cardiac valves, the off-centred approach appears to be more advantageous, since a slightly reduction of the precision on the evaluation of the hydrodynamic forces (but still second order accurate) avoids an increase by a factor 4.63 in computational cost, which would lead to unaffordable simulation (see the numerical test in Section 4).

In conclusion, without the presence of interacting walls, the centred scheme is preferable, since it accounts for a higher order term in the Taylor series of the velocity gradient expansion, even if it requires a larger $h$. On the other hand, the off-centred scheme is convenient when boundaries enclosing thin fluid layers need to be solved. Hence, the most suitable approach will be used in the following numerical tests.

## 4. Results

In the following, the proposed method is tested numerically by computing the hydrodynamic loads of analytical flow solutions, flows around rigid bodies with separation, and FSI for rigid and deformable bodies. As summarised in Table 1, we will consider different orders of the Taylor series for pressure (12a) and viscous stresses (12b): Order 1, when only the leading order term on the right hand side is considered; Order 2, when only the first two terms are retained; and Order $2^+$, when the complete expansion is adopted. We recall that, although in the last case the Taylor-expansion is third order accurate, the accuracy of the corresponding hydrodynamic stresses is limited to second order by the FD scheme and the MLS interpolation used to compute the expansion coefficients. Depending on the application, either the Centred (C) or Off-Centred (OC) methods are used with $h = h_C$ and $h = h_O$, respectively.

### 4.1. Corner flow

In order to test the accuracy of the proposed method, an analytical solution of the Navier-Stokes equations is considered, namely the 2D steady corner flow, which is a prototype of flow over a deformable body, as a membrane bending out of its plane [27]. The flow in the first quadrant ($x_1, x_2 > 0$) with boundary conditions $\mathbf{u}(0, x_2) = U\left[\exp\left(\frac{Ux_2}{\nu}\right) - 1\right]\mathbf{e}_1$ and $\mathbf{u}(x_1, 0) = U\left[\exp\left(\frac{Ux_1}{\nu}\right) - 1\right]\mathbf{e}_2$ is given by:

$$u_1(x_2) = U\left[\exp\left(\frac{Ux_2}{\nu}\right) - 1\right], \quad u_2(x_1) = U\left[\exp\left(\frac{Ux_1}{\nu}\right) - 1\right], \tag{18}$$

with pressure:

$$p(x_1, x_2) = -\rho U^2 \exp\left[-\frac{U}{\nu}(x_1 + x_2)\right], \tag{19}$$

with $U$ a velocity scale, $\rho$ the fluid density and $\nu$ its kinematic viscosity. The streamlines of the corner flow superimposed to the contours of $u_2$ are shown in Fig. 5a.

Differently from flows over rigid bodies, it should be noted that in this case the value of $\partial u_2/\partial x_1$ it is not zero at the $x_2 = 0$ wall, as shown by the contours of $u_2$. Therefore, the tangential stress acting on the lower wall is due to a combination of $\partial u_1/\partial x_2$ and $\partial u_2/\partial x_1$, as it happens over a deformable body. Thus, in this case, the approach proposed in [18,21] cannot be applied, since it overlooks the term $\partial u_2/\partial x_1$ at the wall. In addition, Eq. (10) does not hold true as $\partial p/\partial n$ is not zero on both walls, even if they are not moving.

The square domain $\nu/U[0,1] \times \nu/U[0,1]$ is discretised with $N \times N$ points, assuring a fixed grid size $\Delta$ in both directions. On the horizontal ($x_2 = 0$) wall, Lagrangian markers are distributed with constant spacing $\Delta l = 0.7\Delta$. Wall pressure $p$ and the stress tensor components $\partial u_1/\partial x_2$ and $\partial u_2/\partial x_1$ at the wall obtained with our method are compared against the analytical counterpart.

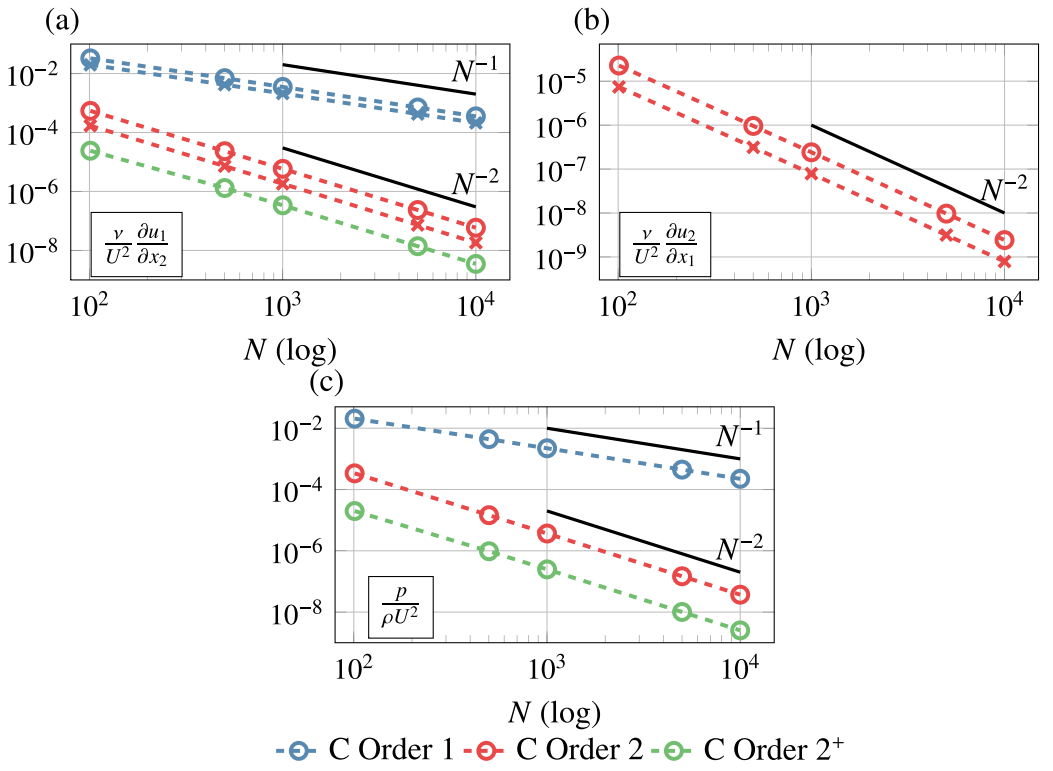


**Fig. 6.** Convergence rate in $L_1$-norm of (a) $\partial u_1/\partial x_2$, (b) $\partial u_2/\partial x_1$ and (c) $p$ at the wall $x_2 = 0$ evaluated with the centre and off-centred version of the proposed method, and for different orders of accuracy. The different line colour refers to the overall accuracy of the method, while the different markers identify the (circle) centred and (crosses) off-centred schemes. The black lines indicate the first and second order of convergence.

Fig. 6a shows in log-log scale the $L_1$ norm of the error on $\partial u_1/\partial x_2$ with respect to the number of grid points $N$, thus confirming that the error of the Order 1 method decreases linearly with the number of points, while the error of Order 2 and 2$^+$ decreases quadratically with $N$. As expected, the most precise method is the centred Order 2$^+$, but interestingly, for the other orders the off-centred approach is more precise with respect to the centred one, owing to the probe closer to the solid wall.

The same plot for $\partial u_2/\partial x_1$ is shown in Fig. 6b, for which all orders behave the same since at the southern wall $\partial^m u_2/\partial n^m = \partial^m u_2/\partial x_2^m = 0$ for $m \geq 1$, leading to $\partial u_2/\partial x_1|_{\mathbf{x}^I} = \partial u_2/\partial x_1|_{\mathbf{x}^P}$. As for $\partial u_1/\partial x_2$, the off-centred approach is slightly more precise. As discussed in Section 3, the Order 2$^+$ of the viscous stresses can be computed in the centred case only.

Pressure loads have the same convergence rate as the velocity gradients (see Fig. 6c), and, as happens for $\partial u_1/\partial x_2$ and $\partial u_2/\partial x_1$, the off-centred scheme applied to Order 1 and 2 is more precise than the centred one.

### 4.2. Stretching plate

Another analytical flow is now considered: the stretching plate, which mimics the flow over a plate stretching at constant rate [27]. The flow for $x_2 > 0$ with boundary condition $\mathbf{u}(x_1, 0) = U^2 x_1/\nu\, \mathbf{e}_1$ is given by:

$$u_1(x_1, x_2) = \frac{U^2 x_1}{\nu} \exp\left(-\frac{U x_2}{\nu}\right), \quad u_2(x_2) = U\left[\exp\left(-\frac{U x_2}{\nu}\right) - 1\right], \tag{20}$$

with the pressure:

$$p(x_2) = -\frac{\rho U^2}{2} \exp\left(-\frac{2U x_2}{\nu}\right), \tag{21}$$

with $U$, $\rho$ and $\nu$ a velocity scale, the fluid density and kinematic viscosity, respectively. The corresponding streamlines of the stretching plate flow superimposed to the contours of $u_1$ are depicted in Fig. 5b. Differently from the corner flow, here the velocity gradient component $\partial u_2/\partial x_1$ is zero at the southern wall, while the $\partial u_1/\partial x_1$ (see Fig. 5b) and $\partial u_2/\partial x_2$ terms are not null, as well as the pressure normal derivative. In the methods based on a field reconstruction near the wall [18,21], the terms $\partial u_1/\partial x_1$ and $\partial u_2/\partial x_2$ are ignored, since only the boundary layer component $\partial u_1/\partial x_2$ can be reconstructed. Furthermore, also in this case $\partial p/\partial n$ is different from zero at the solid fixed wall.

The box $\nu/U[-1/2, 1/2] \times \nu/U[0, 1]$ is uniformly discretized with $N \times N$ points, obtaining a constant grid size $\Delta$, and on the $x_2 = 0$ wall Lagrangian markers are distributed with constant spacing $\Delta l/\Delta = 0.7$.

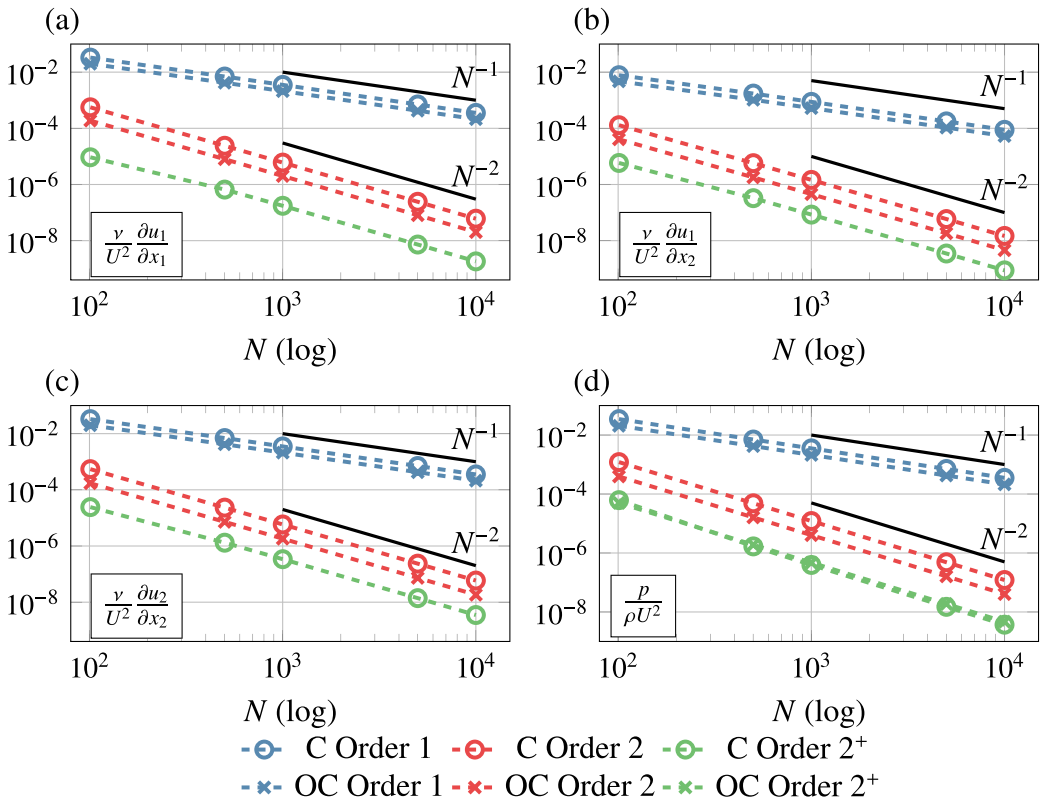


**Fig. 7.** Convergence rate in $L_1$-norm of (a) $\partial u_1/\partial x_1$, (b) $\partial u_1/\partial x_2$, (c) $\partial u_2/\partial x_2$ and (d) $p$ at the wall $x_2 = 0$ evaluated with the centred and off-centred version of the proposed method. The black lines indicate the first and second order of convergence.

The convergence curves of $\partial u_1/\partial x_1$, $\partial u_1/\partial x_2$ and $\partial u_2/\partial x_2$ obtained with the same methods of the corner flow are reported in Fig. 7a–c, respectively. For all components, the off-centred approach performs slightly better for Order 1 and 2 owing to the shorter probe. On the other hand, the error is further decreased when considering the Order $2^+$, which can be only achieved by the centred scheme. The convergence rate of the pressure at the wall is similar to the corner flow case, as shown in Fig. 7d.

### 4.3. Flow around a fixed sphere

We now examine the flow over a stationary sphere. This configuration is of particular interest as it manifests boundary layer separation and, due to its geometrical symmetries, exhibits all possible orientations of the wall normal vector with respect to the coordinate lines. This time, however, an analytical solution is not available and in order to better validate the procedure, we consider the flow solution $\mathbf{u}$ and $p$ obtained from the open-source Finite Elements Method (FEM) library FreeFem++ [28]. In this framework, we can compute the hydrodynamic loads using both FEM and the proposed procedure, hence filtering out possible differences in the underlying flow solver, which would automatically occur when comparing against literature results.

The Reynolds number is based on the velocity of the free stream $U$ and the diameter of the sphere $D$, and we will consider the cases of $Re = 20$ and $Re = 100$, for which the flow is steady and axisymmetric [29]. The axisymmetric steady Navier-Stokes equations are solved in cylindrical coordinates $r - z$ using Taylor-Hood elements within a $12 \times 6$ rectangle.

The sphere is represented by an arc of circumference placed on the symmetry axis and the mesh is progressively refined as approaching the body. A Dirichlet boundary condition is used to impose a uniform inflow velocity, while on the lateral and outflow boundaries free-stress conditions are imposed. Symmetry conditions are imposed on the axis.

Pressure $C_P$ and viscous $C_V$ drag coefficients, together with the total drag coefficient $C_D = C_P + C_V$, are evaluated from the body fitted simulation calculating the line integrals with a Gaussian quadrature formula of order 1. From the same simulation, the pressure distribution over the sphere along with the viscous stress tensor component $\tau_{\rho\theta}$ are extracted. The corresponding stress distribution and force coefficients are shown in Fig. 8 and Table 2, respectively, denoted as FEM/FEM to recall that both the flow solution and the loads computation are carried out using the FEM library.

On the other hand, to evaluate the hydrodynamic stresses with the proposed method (centered version), a set of Lagrangian markers is distributed in correspondence of the FEM nodes located on the surface of the sphere. Thus, 180 equispaced markers with stride $\Delta l = 0.0087$ are considered, and the corresponding probes points $\mathbf{X}^P$ are placed at a distance $h_C = 2.5\sqrt{2}\,\Delta l$ from the markers.

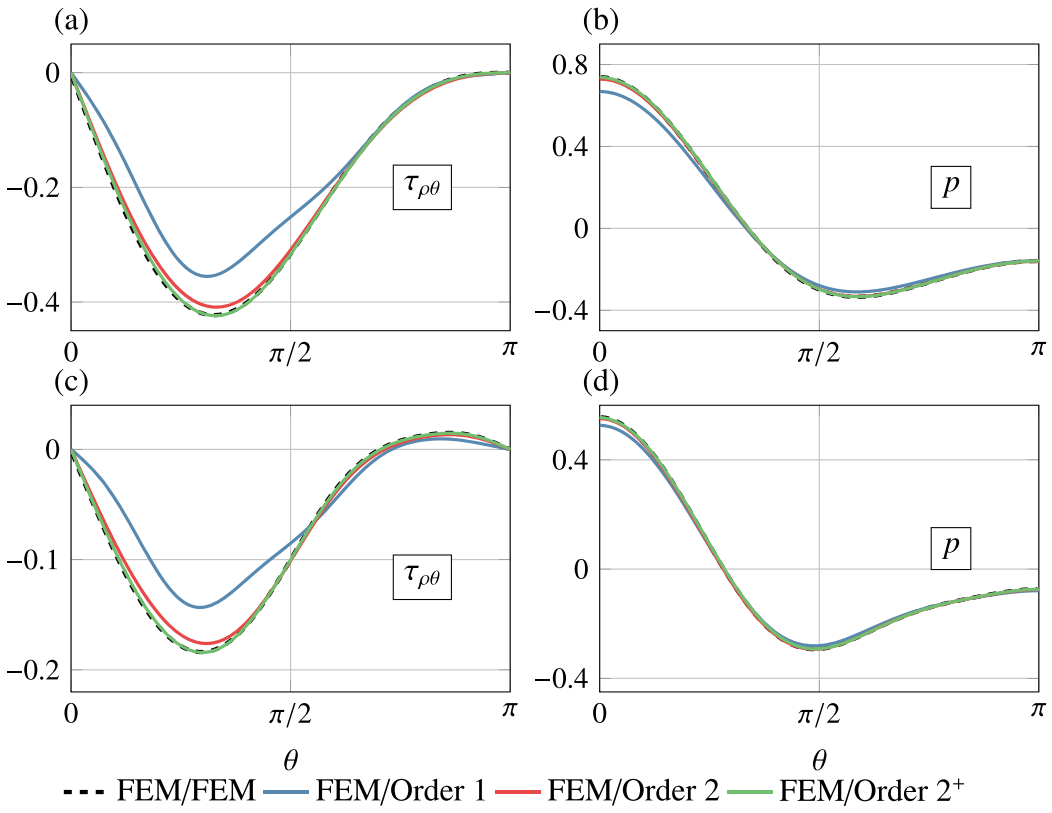


**Fig. 8.** (a) Viscous stress $\tau_{\rho\theta}$ and (b) pressure distribution over the surface of the sphere obtained with Order 1, 2 and $2^+$ for the case $Re = 20$, compared with the FEM results. $\rho = \sqrt{r^2 + z^2}$ is the radial distance from the sphere centre and $\theta = \tan^{-1}(r/z)$ is the corresponding azimuthal coordinate (with $\theta = 0$ and $\theta = \pi$ the leading and trailing edge, respectively). Panels (c) and (d) show the same quantities for $Re = 100$.

The flow velocity and pressure are then sampled over the Eulerian point $\mathbf{x}^k$ of the MLS supporting domain of the probes. Finally, the stresses are obtained as detailed in Section 3 and denoted as FEM/Order 1, 2, $2^+$, depending on the order chosen.

With respect to the FEM/FEM solution, all the orders describe the correct qualitative behaviour of $\tau_{\rho\theta}$ at $Re = 20$, as shown in Fig. 8a, even if FEM/Order 1 deviates from the reference solution near the minimum of $\tau_{\rho\theta}$. The viscous stress precision is enhanced when using FEM/Order 2, although a slight overestimation of the minimum value of $\tau_{\rho\theta}$ remains. On the contrary, the viscous stress obtained with Order $2^+$ reproduces well the result of the FEM/FEM simulation over the whole surface of the sphere, being the two curves superimposed. Furthermore, the distribution of pressure is well captured by all the orders, as shown in Fig. 8b. In particular, FEM/Order 1 slightly underestimates the pressure at the frontal stagnation point and overestimates the minimum of $p$, while the curves obtained with FEM/Order 2 and FEM/Order $2^+$ overlap to the reference FEM/FEM simulation. The same behaviour is observed at $Re = 100$, as confirmed by Fig. 8c and d.

The corresponding pressure $C_P$ and viscous $C_V$ drag coefficients are reported in Table 2. For $Re = 20$, the viscous drag coefficient predicted by FEM/Order 1 is underestimated by 13% with respect to the FEM/FEM simulation, while the error for FEM/Order 2 is 1.4%, which is further reduced up to 0.6% when FEM/Order $2^+$ is employed. For the pressure, the $C_P$ value of FEM/Order 1 is slightly below the FEM/FEM reference value. This discrepancy is progressively reduced if FEM/Order 2 or FEM/Order $2^+$ are employed, confirming the results of Fig. 8b. Similar conclusions apply to the case $Re = 100$. In the same table we also report the values obtained by applying the method to the 3D flow solution coming from the IB solver described in Section 2, using a $12 \times 12 \times 12$ computational domain uniformly discretised by $1000 \times 1000 \times 1000$ points. The results are within 2% with respect to the literature and the FEM/FEM solution.

### 4.4. Sedimentation of oblate spheroid

We now consider the sedimentation of an oblate spheroid (i.e. the solid obtained from the revolution of an ellipse around its minor axis, see Fig. 9a, immersed in a viscous fluid initially at rest under the effect of gravity. The spheroid is made of a uniform material of density $\rho_b$, with $d$ and $a$ the lengths of its major and minor axes, respectively. The body-to-fluid density ratio $\gamma = \rho_b/\rho$ is fixed to 2.14, while the aspect ratio $\chi = d/a$ is set to 1.5. The Galileo number $Ga = \rho U_g d/\mu$, i.e. the Reynolds number based on the gravitational velocity $U_g = \sqrt{\pi(\gamma - 1)\tilde{g}d/6\chi}$, being $\tilde{g} \simeq 9.81\,\mathrm{m/s^2}$ the gravitational acceleration, is varied to test the capability of the

**Table 2**
Coefficients of viscous $C_V$, pressure $C_P$ and total $C_D$ drag at $Re = 20$ and $Re = 100$ for the flow around the sphere. The labels FEM/Order 1, 2, $2^+$ refer to the coefficients calculated using the pressure and velocity fields obtained from the FEM simulation and then applying our method (centered version), while the FEM/FEM label refers to the loads extracted directly from the FEM simulation. IB/Order 1, 2, $2^+$ correspond to the force coefficients obtained by applying our method to the 3D IB simulations. The force coefficients computed numerically using a body-fitted fluid solver by [30] are also reported.

| | $Re = 20$ | | | $Re = 100$ | | |
|---|---|---|---|---|---|---|
| | $C_V$ | $C_P$ | $C_D$ | $C_V$ | $C_P$ | $C_D$ |
| FEM/Order 1 | 1.489 | 0.927 | 2.416 | 0.478 | 0.486 | 0.964 |
| FEM/Order 2 | 1.687 | 1.011 | 2.697 | 0.577 | 0.501 | 1.078 |
| FEM/Order $2^+$ | 1.700 | 1.021 | 2.721 | 0.574 | 0.512 | 1.086 |
| FEM/FEM | 1.705 | 1.024 | 2.729 | 0.577 | 0.513 | 1.091 |
| IB/Order 1 | 1.390 | 0.893 | 2.282 | 0.426 | 0.488 | 0.911 |
| IB/Order 2 | 1.701 | 1.015 | 2.716 | 0.594 | 0.494 | 1.088 |
| IB/Order $2^+$ | 1.732 | 1.041 | 2.773 | 0.593 | 0.516 | 1.111 |
| Ref. [30] | 1.721 | 0.986 | 2.707 | 0.584 | 0.508 | 1.092 |

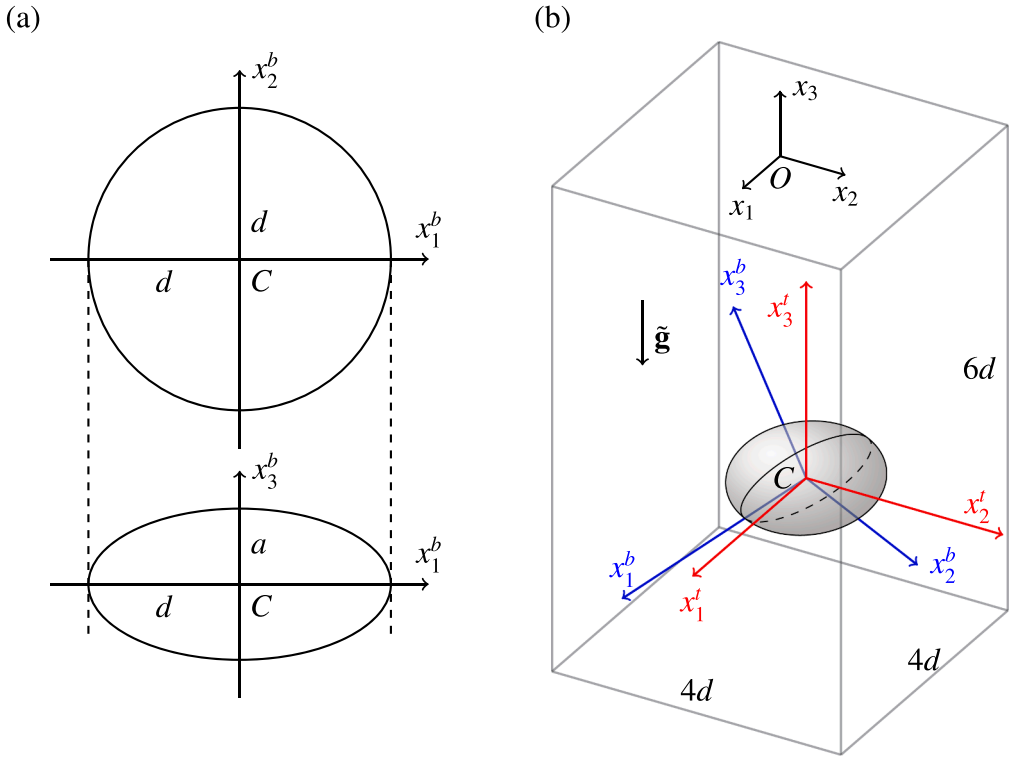


**Fig. 9.** (a) Detail of the spheroid geometrical properties: $d$ is the length of the spheroid major axes, while $a$ is the length of the spheroid minor axis. (b) Sketch of the computational domain used for the sedimentation of the oblate spheroid, together with the three reference frame used for this test case: in black the inertial frame, in blue the body fixed frame and in red the fluid frame. The gravity vector $\tilde{\mathbf{g}}$ is aligned with the vertical direction $x_3$. (For interpretation of the references to colour in this figure legend, the reader is referred to the web version of this article.)

method to describe different FSI regimes. Thus, in the following, the method is employed to analyse the case $Ga = 150$, corresponding to a vertical periodic (VP) terminal falling, and the case $Ga = 110$ , where the spheroid is expected to reach a steady oblique (SO) path [31,32]. As will be shown later, this latter case is particularly challenging since the system is close to the transition threshold from the SO to the VP path [32], thus the precise evaluation of the loads is key to describe the correct behaviour of the system.

An inertial frame of reference $Ox_1x_2x_3$, with $x_3$ aligned with the gravity vector $\tilde{\mathbf{g}}$, is introduced along with a reference frame fixed with the body principal axes $Cx_1^bx_2^bx_3^b$, being $C$ the centre of the spheroid (see Fig. 9b). The rigid body dynamics, made non-dimensional using $d$, $U_g$ and $\rho$, is governed by the Newton equations for the position $\mathbf{r}$, velocity $\mathbf{v}$ and acceleration $\mathbf{a}$ of the

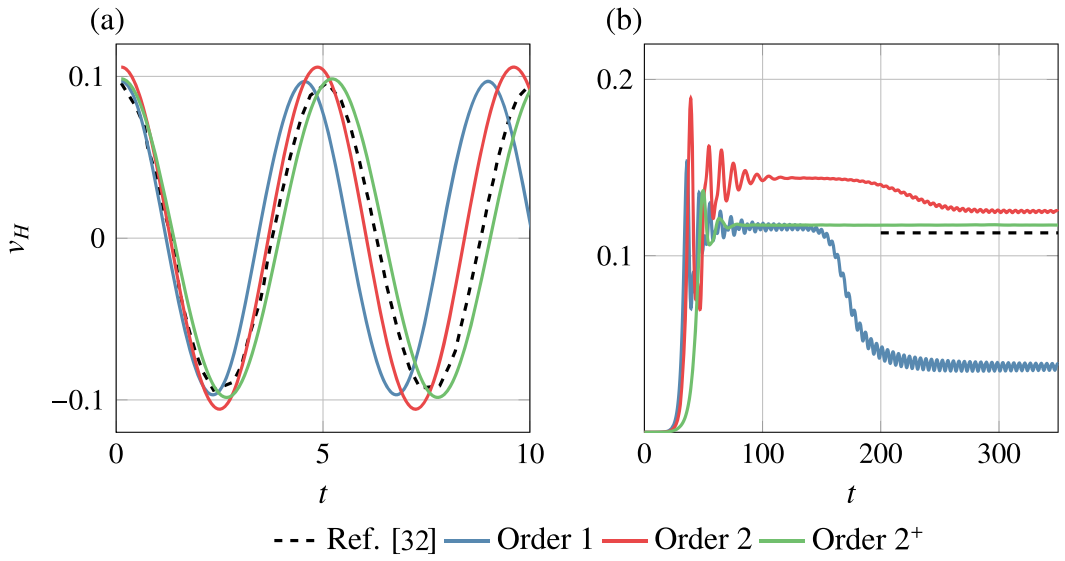


**Fig. 10.** Horizontal velocity of the spheroid for the (a) VP and (b) SO path obtained with (centred) Order 1, 2 and 2⁺. For a better comparison against the results of [32], all curves in (a) have been aligned to have their maximum in $t = 0$.

**Table 3**
Comparison of the VP regime metrics evaluated with the proposed method (centred version), against the reference values from [32].

| | $St$ | $v'_H$ | $\bar{v}_V$ | $v'_V$ | $Re_V$ |
|---|---|---|---|---|---|
| Order 1 | 0.226 | 0.194 | 1.829 | 0.0078 | 274 |
| Order 2 | 0.211 | 0.211 | 1.814 | 0.0021 | 272 |
| Order 2⁺ | 0.196 | 0.197 | 1.738 | 0.0035 | 261 |
| Ref. [32] | 0.198 | 0.194 | 1.740 | 0.0038 | 261 |

**Table 4**
Comparison of the SO regime metrics evaluated with the proposed method (centred Order 2⁺) against the reference values from [32].

| | $v_H$ | $v_V$ | $Re_V$ | $\alpha(^\circ)$ | $\varphi(^\circ)$ |
|---|---|---|---|---|---|
| Order 2⁺ | 0.117 | 1.639 | 180 | 4.097 | 4.999 |
| Ref. [32] | 0.113 | 1.682 | 185 | 3.842 | 5.318 |

centre of the body, while the Euler equations determine the angular velocity $\boldsymbol{\omega}$ of the body. The orientation of the spheroid is described by quaternions [33] and Navier-Stokes equations are solved in a non-inertial reference frame $Cx'_1x'_2x'_3$ with axis parallel to $x_1$, $x_2$ and $x_3$ but with the origin fixed with the body centre $C$.

A loose coupling approach is adopted to advance in time the fluid and the structural part, solving the Newton-Euler and the quaternions equations with a three-stage explicit Runge-Kutta method, normalising at each sub-step the quaternions to assure a unitary norm. Normalizing lengths by $d$ and velocities by $U_g$, the fluid computational domain is a $4 \times 4 \times 6$ box, discretised using $200 \times 200 \times 300$ points in each direction, for a uniform grid spacing $\Delta = 0.02$, while the time step is kept fixed to $\Delta t = 10^{-4}$. At the inflow (at a distance 2 from $C$), a non-inertial Dirichlet boundary condition $\mathbf{u} = -\mathbf{v}$ is imposed.

For the case at $Ga = 150$, all the orders describe correctly the limit-cycle of the system [32], as confirmed by the horizontal velocity at regime shown in Fig. 10a. As shown in Table 3, Order 1 overestimates the oscillation frequency $St$ with respect to the reference data, while Order 2 reduces the error on $St$, but at the same time overestimates the amplitude $v'_H$ of the horizontal velocity. Instead, Order 2⁺ correctly captures the oscillation of $v_H$, both in frequency and in amplitude. Concerning the vertical velocity, Order 1 and Order 2 slightly overestimate the mean falling velocity $\bar{v}_V$ and the corresponding Reynolds number $Re_V = Ga\,\bar{v}_V$, even if the amplitude of oscillation $v'_V$ provided by the former method is way larger than the reference value, while $v'_V$ is underestimated by Order 2. In contrast, Order 2⁺ describes the vertical velocity and $Re_V$ with an error below the 2% with respect to the literature data [32].

On the contrary, for the SO regime ($Ga = 110$), the vertical velocity $v_H$ should reach a constant value [32], but Order 1 and 2 attain a periodic regime, oscillating with a mean velocity different from the expected steady value, as shown in Fig. 10b. On the

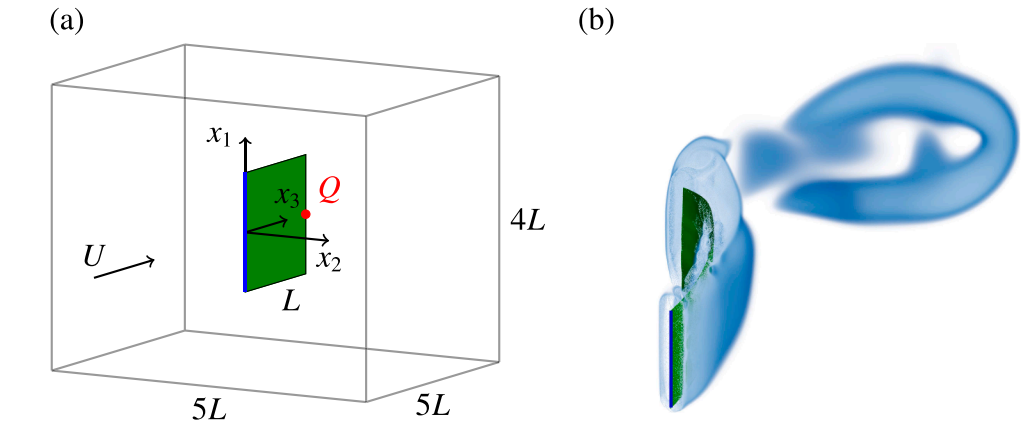


**Fig. 11.** (a) Numerical setup for the flow around the flapping flag. The blue segment indicates the pinned leading edge of the flag, while the Lagrangian point $Q$ is placed at the mid-point of the trailing edge of the flag. (b) Typical hairpin vortical structure behind the flag visualised with the Q-criterion. (For interpretation of the references to colour in this figure legend, the reader is referred to the web version of this article.)

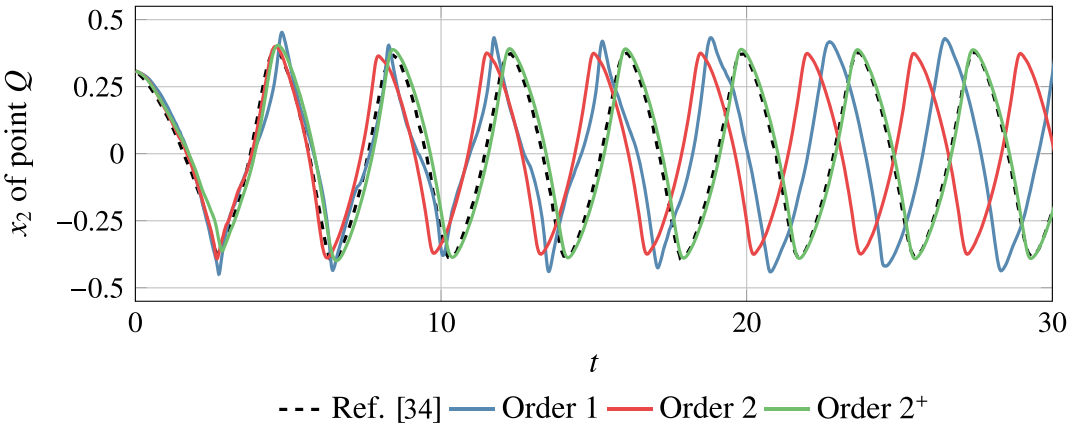


**Fig. 12.** Time evolution of the $x_2$ coordinate of the trailing-edge point $Q$ in Fig. 11 obtained with the (centred) Order 1,2 and $2^+$. The curves are compared with the result presented in [34].

**Table 5**
Comparison of the peak to peak amplitude $A$ and Strouhal number $St$ of the periodic oscillation of the trailing-edge point $Q$ of the flag evaluated with the (centred) Order 1, 2 and $2^+$.

| | Order 1 | Order 2 | Order $2^+$ | Ref. [17] | Ref. [34] |
|---|---|---|---|---|---|
| Amplitude $A$ | 0.858 | 0.749 | 0.779 | 0.795 | 0.780 |
| Strouhal number $St$ | 0.274 | 0.287 | 0.264 | 0.265 | 0.260 |

other hand, the long time behaviour of the system is correctly captured by Order $2^+$, and the horizontal $v_H$ and vertical $v_V$ terminal velocities along with the corresponding Reynolds number $Re_V = Ga\, v_V$ are within 5% to the reference results (see Table 4). The geometrical angles $\alpha$ and $\varphi$, respectively formed between the terminal velocity of the body and the $x_3^b$ axis with respect to $x_3$, also compare well with the literature.

### 4.5. Flow around a flapping flag

We now focus on the FSI of the flow around a deformable square flag pinned at the leading edge, as shown in Fig. 11a. The reference velocity and length are, respectively, the free-stream velocity $U$ and the length of the flag edge $L$. The flag has thickness $s = 0.01\,L$ and it is made of an inextensible linear-elastic uniform material of density $\rho_b = 100\,\rho$ with bending modulus $B = 10^{-4}\,\rho\,U^2\,L^3$. The Reynolds number based on $U$ and $L$ is $Re = 200$.

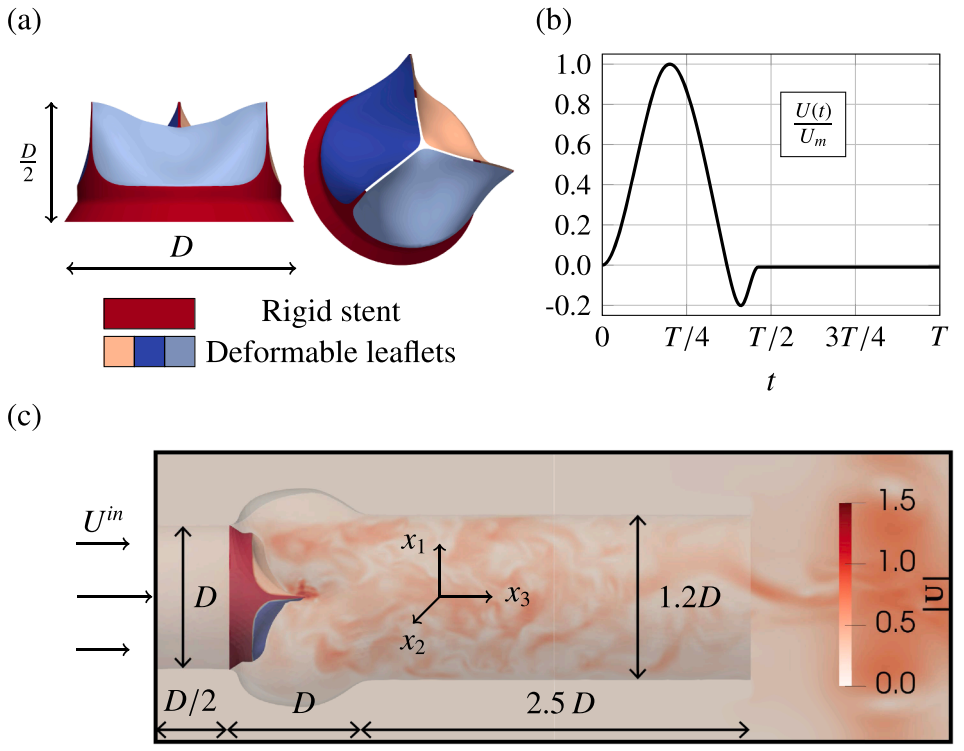


**Fig. 13.** (a) Detail of the prosthetic aortic valve. (b) Temporal profile $U(t)$ of the inflow within one period. (c) Sketch of the computational domain employed together with the geometrical dimension of the rigid aortic root. In background it is shown a slice on the $x_1 - x_3$ plane of the isocontours of the velocity magnitude during diastole (aortic valve in the closed configuration, $t = 1.44T$) obtained with the off-centred scheme.

The flag is treated as a 2D surface immersed in a 3D flow, and its structural dynamics is described using the spring-mass network approach detailed in [17], loosely coupled with the flow solver. To replicate the inextensibility of the flag, a large Young modulus is prescribed to the spring-mass model, namely $E = 10^3\,\rho\,U^2\,L/s$.

In non-dimensional units, the computational domain is a box of dimension $4 \times 5 \times 5$, discretised by $200 \times 250 \times 250$ grid points, using a constant grid size of $\Delta = 0.02$. The time step is equal to $\Delta t = 10^{-4}$. The flag is initially planar, with the leading edge at a distance 2 from the inlet, tilted by an angle $\theta_0 = 0.1\pi$ with respect to the $x_1 - x_3$ plane.

For the chosen parameters the system reaches a periodic regime [34], where an alternating shedding of hairpin vortices from the trailing edge is present (see Fig. 11b). In Fig. 12 is shown the time evolution of the $x_2$ coordinate of the mid-point of the trailing edge of the flag (point $Q$ of Fig. 11a) since the initial time up to the attainment of the periodic regime, obtained with all the orders (centred approach) and compared with data from the literature [17,34]. The Order 1 method clearly overestimates the amplitude of oscillations, while Order 2 predicts correctly the onset of the instability, but provides a slightly higher oscillation frequency at regime with respect to the reference data. Lastly, Order $2^+$ is able to correctly describe the transient phase and the long term behaviour of the flag.

In Table 5, the corresponding peak to peak amplitude $A$ and the Strouhal number $St$ at regime are reported for all the cases, along with the data from literature.

### 4.6. Haemodynamics through the aortic valve

Let now consider the case of multiple deformable bodies interacting among each other via thin fluid gaps. In this scenario, the FSI is governed by the hydrodynamic loads generated within these lubrication layers, and the length of the probe used by the method becomes a computational bottleneck as it should be smaller than half the width of the gap (as previously sketched in Fig. 4). Hence, in this case the off-centred approach introduced in Section 3 might be preferred, and we wish to compare it against the centred approach.

A representative example for this class of problems is the flow through a biological prosthetic aortic valve shown in Fig. 13a, which is mounted within a straight tract of aorta. The valve is made of a rigid stent and three deformable leaflets which passively open during systole, corresponding to the inflow peak in Fig. 13b. Importantly, during diastole, when the valve is closing, the aortic leaflets approach each other until they coapt at their tips, effectively sealing and blocking blood flow through the closed valve, as shown in Fig. 13c together with the numerical setup employed.

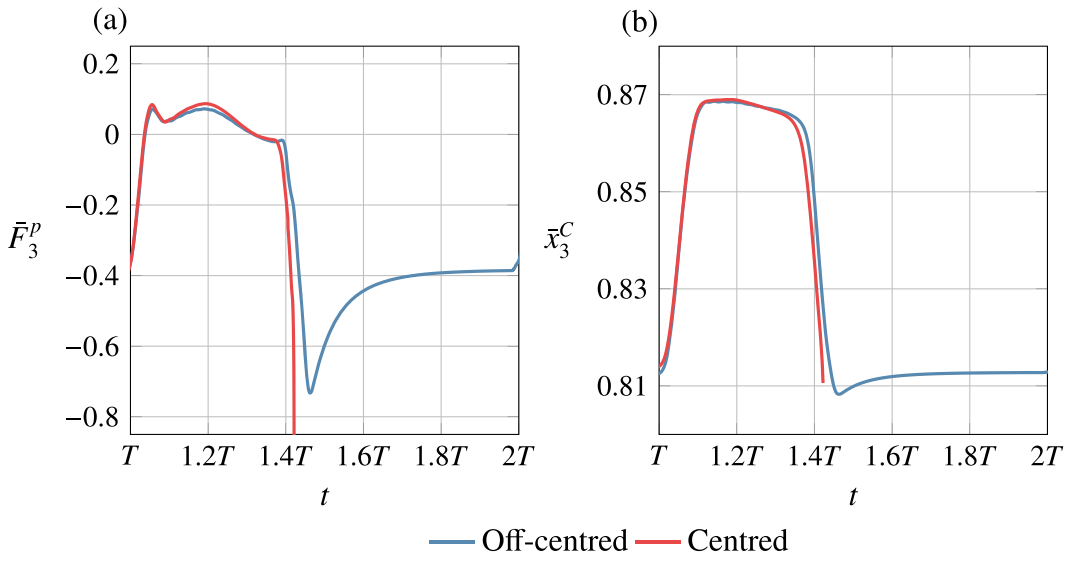


**Fig. 14.** (a) $x_3$ component of the mean value among the three leaflets of the net pressure force. (b) $x_3$ component of the mean value among the three leaflets of the position of the centre of the leaflets.

At the inlet of the aorta we impose a pulsatile flow along the $x_3$ direction $U_{in}(t,r) = U(t)\tanh\left[20(1-2r/D)\right]/\tanh(20)$, with $r = \sqrt{x_1^2 + x_2^2}$ and $U(t)$ the periodic profile reported in Fig. 13b for one period. The reference length and velocity are the aortic root diameter $D = 21$ mm and the inflow peak velocity $U_m = 0.5$ m/s, respectively. The Reynolds number based on $D$ and $U_m$ is $Re = 3180$, and the non-dimensional period of the flow is $T = 17.86$ (corresponding to an heart rate of 60 b.p.m.). The leaflets are treated as 2D surfaces made of a linear elastic material of density $\rho_b = \rho$ and thickness $s = 2.5 \times 10^{-2}\, D$. The Young modulus of the leaflets is $E = 25\,\rho U_m^2 D/s$ and the bending modulus is $B = 10^{-3}\,\rho U_m^2 D^3$. The structural dynamics is solved using the spring-mass network approach of [17], as done for the flag case, while the details of the contact model can be found in [35]. The computational domain in non-dimensional units is a box of dimension $2 \times 2 \times 5.5$, and the symmetry axis of the aorta is aligned with the $x_3$ direction, placed at the centre of the box. An unsteady Dirichlet boundary condition is used to impose $U_{in}$ at the inlet of the aorta. The fluid domain is discretised with a uniform Eulerian mesh made of $200 \times 200 \times 550$ points, for a constant grid spacing of $\Delta = 0.01$, and $\Delta t = 5 \times 10^{-5}$.

In order to analyse the effect of the probe length on the FSI of the leaflets, both centred and off-centred cases are considered. Specifically, Order $2^+$ is used to evaluate pressure in both cases, while the velocity gradients are evaluated with Order $2^+$ for the centred approach and with Order 2 for the off-centred approach. The length of the probe $h$ is equal to $h_C = 2.5\sqrt{3}\Delta$ in the first case and to $h_O = 1.5\sqrt{3}\Delta$ in the latter case.

During the systolic phase (positive $U$), a pressure drop opens the valve and drives the flow from the inlet to the outlet. Then, given the backflow imposed at the inlet (diastolic phase), the pressure gradient is inverted across the aorta, eventually closing the valve and stopping the flow through it. The valve remains closed until the end of the cardiac period, when the positive inflow will open the valve again. A snapshot of the velocity magnitude in the $x_1 - x_3$ plane obtained with the off-centred scheme at $t = 1.44\,T$ (during diastole), when the valve is completely closed and the leaflets are in contact among them, is shown in Fig. 13c.

The $x_3$ component of the net pressure force $\bar{F}_3^p$ (averaged among the three leaflets) computed using both the centred and off-centred formulations is shown in Fig. 14a. Before starting the closing process, the two methods predict the same pressure force on the leaflets. However, as soon as the leaflets are approaching, the pressure force predicted by the centred scheme diverges, stopping the simulation, while the off-centred scheme is able to evaluate the forces during the pre-contact and contact phase and it manages to reopen the valve. Interestingly, the curve of the centred scheme is slightly shifted to the left (smaller times) near the contact instant, since in this case the leaflets feel the others in advance with respect to the off-centred scheme, given the larger $h$. A similar behaviour is observed in Fig. 14b, where the streamwise component of the centre of the leaflets $\bar{x}_3^C$ (averaged among the three leaflets) is shown.

The premature ending of the centred simulation is due to the larger supporting domain required for the evaluation of the stresses associated to each Lagrangian marker with respect to the off-centred approach. Thus, when the leaflets are close each other the centred approach is not able to evaluate correctly the hydrodynamics loads, since some points of the such supporting domain are not within the thin fluid region between the leaflets.

From the above results, it is clear that in presence of narrow fluid gaps or deformable bodies approaching each other, the off-centred scheme can be advantageous as it allows to use a coarser grid with respect to the centred approach (see Fig. 4), still provided that the corresponding numerical precision is suitable for the given application. Nevertheless, the centred method, having a higher precision, can still be used, but it entails a larger computational cost owing to the smaller grid size needed to accommodate the longer probe and the corresponding supporting domain points required for the evaluation of the traction within the fluid gap.

## 5. Conclusions

In this work, a novel and accurate method to evaluate the hydrodynamic loads acting on deformable bodies is presented in the framework of FSI simulation with direct forcing IBM. The proposed method improves former approaches employed in IBM solvers for deformable bodies, which are only first order accurate [12,17]. On the other hand, higher order methods proposed in the literature are mostly limited to rigid bodies and rely on the assumption of boundary layer flows [18,21].

The first step of our method is a truncated Taylor-series expansion of the whole stress tensor from a probe point, located within the fluid bulk, backward to the surface of the body. In general, the probe location does not coincide with an Eulerian point, thus it is necessary to interpolate pressure, velocity and their derivatives from the grid points surrounding the probe. To accomplish that, the same MLS kernels used in the IB forcing step are used for the interpolation from the fluid to the probe, guaranteeing a smooth evaluation of the loads. In particular, the first and second derivatives of pressure and velocity are evaluated on the Eulerian grid with a centred FD approximation and then interpolated to the probe location. On the contrary, the third derivative of velocity is evaluated exploiting the first derivative of the MLS basis functions (applied to the velocity second derivatives). Therefore, with our method the second order accuracy of the fluid solver is preserved in the evaluation of the stresses. Furthermore, since the full stress tensor is tracked, the method is able to cope with deformable surfaces where all the stress components may be not null.

This novel approach has been tested numerically against several benchmark cases. The order of accuracy of the method has been verified using two analytical solutions of the Navier-Stokes equations with boundary conditions mimicking a fluid/solid interface between a deformable solid and a fluid. Then, the precision of the method has been investigated in flows with massive separation and in the FSI of rigid and deformable bodies. Furthermore, the problem of narrow gaps and contact between walls has been tackled, proposing an alternative method for the estimation of the Taylor-series coefficients using off-centred FD approximation for the Eulerian derivatives, thus retaining a smaller supporting domain for the evaluation of the traction. In all the numerical experiments considered, the computational overhead of the method is below 8%.

Although the proposed method has been derived and validated for incompressible low-Reynolds-number flows, its extension to compressible regimes is straightforward. In particular, compressibility effects can be incorporated into the method by accounting for the volumetric stress term proportional to $(\nabla \cdot \mathbf{u})\boldsymbol{I}$. The divergence of the velocity field can be evaluated on the Eulerian grid by using the centred FD approximation, obtaining a field analogous to the pressure. Thus, the same Taylor-series expansion and MLS interpolation employed for the pressure can be applied to the volumetric stress.

The method has been introduced in the framework of direct forcing IBM, but it can be implemented in any CFD solver, even not based on IBM. For instance, in one of the test cases reported here, it has been employed to evaluate the hydrodynamic loads acting on a fixed sphere using the pressure and velocity fields obtained from a body-fitted FEM solution. As a last note, the mixed MLS-Taylor boundary reconstruction could be employed not only to evaluate the hydrodyanmics loads, but also in the dual problem of enforcing immersed boundary conditions. This approach would bear similarities with the shifted boundary method proposed in isogeometric analysis [36], where the boundary condition values are shifted by means of high-order Taylor expansions to preserve optimal accuracy and circumvents the small cut-cell problem.

### CRediT authorship contribution statement

**Giovanni Vagnoli:** Conceptualization, Data curation, Formal analysis, Investigation, Methodology, Software, Validation, Visualization, Writing – original draft; **Martino A. Scarpolini:** Data curation, Investigation, Methodology, Software, Validation, Visualization; **Roberto Verzicco:** Investigation, Methodology, Supervision, Writing – review & editing; **Francesco Viola:** Conceptualization, Funding acquisition, Investigation, Methodology, Project administration, Resources, Writing – review & editing, Supervision.

### Data availability

Data will be made available on request.

### Declaration of competing interest

The authors declare that they have no known competing financial interests or personal relationships that could have appeared to influence the work reported in this document

### Acknowledgements

This project has received funding from the European Research Council under the European Union's Horizon Europe research and innovation program (Grant No. 101039657, CARDIOTRIALS to F.V.).

### Appendix A. Moving least squares kernels

To build the MLS kernels $\phi_k$ for a generic point $\mathbf{X}$, a supporting domain centred on the point $\mathbf{X}$ containing $N_E$ Eulerian points $\mathbf{x}^k$ is created. Typically, 3 points are considered in each spatial direction, for a total of 27 points in 3D and 9 points in 2D (see Fig. 2).

Given a generic Eulerian field $u$, its interpolation $U$ on the point $\mathbf{X}$ is given by:

$$U(\mathbf{X}) = \mathbf{p}^T(\mathbf{X})\mathbf{a}(\mathbf{X}) = \sum_{j=1}^{m} p_j(\mathbf{X})a_j(\mathbf{X}), \tag{A.1}$$

where $\mathbf{p} \in \mathbb{R}^m$ is the vector of polynomial basis functions of degree at most $m$. The unknown interpolation coefficients $\mathbf{a} \in \mathbb{R}^m$ are obtained upon minimisation of the following $L_2-$ weighted norm:

$$J = \sum_{k=1}^{N_E} W\left(\mathbf{X} - \mathbf{x}^k\right)\left[\mathbf{p}^T\left(\mathbf{x}^k\right)\mathbf{a}(\mathbf{X}) - u\left(\mathbf{x}^k\right)\right]^2, \tag{A.2}$$

being $W$ the weight function and $J$ the cost function to be minimised. Imposing the minimisation condition $\partial J/\partial a_j = 0$, $j = 1, \dots, m$, leads to the following $m \times m$ linear system of equations:

$$A(\mathbf{X})\mathbf{a}(\mathbf{X}) = B(\mathbf{X})\mathbf{u}, \tag{A.3}$$

with

$$A(\mathbf{X}) = \sum_{k=1}^{N_E} W\left(\mathbf{X} - \mathbf{x}^k\right)\mathbf{p}\left(\mathbf{x}^k\right)\mathbf{p}^T\left(\mathbf{x}^k\right) \quad \in \mathbb{R}^{m\times m}, \tag{A.4}$$

$$B(\mathbf{X}) = \left[W\left(\mathbf{X} - \mathbf{x}^1\right)\mathbf{p}\left(\mathbf{x}^1\right), \dots, W\left(\mathbf{X} - \mathbf{x}^{N_E}\right)\mathbf{p}\left(\mathbf{x}^{N_E}\right)\right] \quad \in \mathbb{R}^{m\times N_E}, \tag{A.5}$$

$$\mathbf{u} = \left[u\left(\mathbf{x}^1\right), \dots, u\left(\mathbf{x}^{N_E}\right)\right]^T \quad \in \mathbb{R}^{N_E}. \tag{A.6}$$

In this work, consistently with the second order accuracy of the fluid solver, we choose $m = 3$ and $\mathbf{p}(\mathbf{x}) = \left[1, x_1, x_2\right]^T$ for 2D flows and $m = 4$ and $\mathbf{p}(\mathbf{x}) = \left[1, x_1, x_2, x_3\right]^T$ for 3D. The vector $\boldsymbol{\gamma}^T(\mathbf{X}) = \mathbf{p}^T(\mathbf{X})A^{-1}(\mathbf{X})$ is introduced along with the MLS basis function vector:

$$\boldsymbol{\Phi}(\mathbf{X}) = \mathbf{p}^T(\mathbf{X})A^{-1}(\mathbf{X})B(\mathbf{X}) = \boldsymbol{\gamma}^T(\mathbf{X})B(\mathbf{X}) \in \mathbb{R}^{N_E}, \tag{A.7}$$

such that the MLS kernels $\phi_k(\mathbf{X})$ is the $k$th component of $\boldsymbol{\Phi}(\mathbf{X})$. Therefore, the interpolation (A.1) of the field $u$ on the point $\mathbf{X}$ recasts as:

$$U(\mathbf{X}) = \boldsymbol{\Phi}^T(\mathbf{X})\mathbf{u} = \sum_{k=1}^{N_E} \phi_k(\mathbf{X})u\left(\mathbf{x}^k\right). \tag{A.8}$$

The weight functions here considered are given by the product of one dimensional exponential functions:

$$W(\mathbf{r}) = W_1(r_1)W_2(r_2)W_3(r_3), \quad W_i(r) = \begin{cases} \exp\left[-\left(\frac{r}{\varepsilon H_i}\right)^2\right] & r \le H_i, \\ 0 & r > H_i. \end{cases} \tag{A.9}$$

The parameter $H_i$ is the dimension of the supporting domain in the $i$th spatial direction, which is equal to $3/2\Delta x_i$ if 3 points per direction are chosen, while $\varepsilon$ is a shape parameter, which allows modifying how peaked the MLS functions are around the Lagrangian marker, here fixed to 0.7. Notice that, with the employment of this weight functions, the MLS kernels $\phi_k$ are build independently of the particular underlying field $u$: indeed, the kernels depend only on the relative position of the interpolation point $\mathbf{X}$ and of the Eulerian points $\mathbf{x}^k$ contained on its supporting domain. Therefore, once the $\phi_k$ are evaluated for a specific interpolation point, they can be used to interpolate any Eulerian field.

The MLS derivative of the interpolated field $U$ on the point $\mathbf{X}$ is obtained by differentiation of Eq. (A.8):

$$\left.\frac{\partial U}{\partial x_r}\right|_{\mathbf{X}} = \left(\left.\frac{\partial \boldsymbol{\Phi}}{\partial x_r}\right|_{\mathbf{X}}\right)^T \mathbf{u} = \sum_{k=1}^{N_E} \left.\frac{\partial \phi_k}{\partial x_r}\right|_{\mathbf{X}} u\left(\mathbf{x}^k\right). \tag{A.10}$$

The derivative of the MLS kernels $\partial\boldsymbol{\Phi}/\partial x_r$ can be obtained by differentiation of Eq. (A.7):

$$\left.\frac{\partial \boldsymbol{\Phi}}{\partial x_r}\right|_{\mathbf{X}} = \left.\frac{\partial \boldsymbol{\gamma}^T}{\partial x_r}\right|_{\mathbf{X}} B(\mathbf{X}) + \boldsymbol{\gamma}^T(\mathbf{X})\left.\frac{\partial B}{\partial x_r}\right|_{\mathbf{X}}. \tag{A.11}$$

Since $\mathbf{p} = A\boldsymbol{\gamma}$, the derivative of $\boldsymbol{\gamma}$ is the solution of the following $m \times m$ linear system of equations [25]:

$$A(\mathbf{X})\left.\frac{\partial \boldsymbol{\gamma}}{\partial x_r}\right|_{\mathbf{X}} = \left.\frac{\partial \mathbf{p}}{\partial x_r}\right|_{\mathbf{X}} - \left.\frac{\partial A}{\partial x_r}\right|_{\mathbf{X}} \boldsymbol{\gamma}(\mathbf{X}). \tag{A.12}$$

## Appendix B. Centred and off-centred finite differences scheme

The terms of Taylor-expansion of Eq. (12) are built obtained by the MLS interpolation of the pressure and velocity derivatives from the Eulerian grid to the probe location $\mathbf{X}^P$. Thus, a fundamental step of the method is the correct evaluation of the derivatives of $p$ and $\mathbf{u}$ on the Eulerian points lying within the supporting domain of interpolation of $\mathbf{X}^P$. In Section 3, two alternative strategies to evaluate such derivatives are proposed, the centred and the off-centred approach. The two approaches are shown in Fig. B.1 for a 2D uniform grid of spacing $\Delta$, where the supporting domain for the MLS interpolation is made of $N_E = 9$ points.

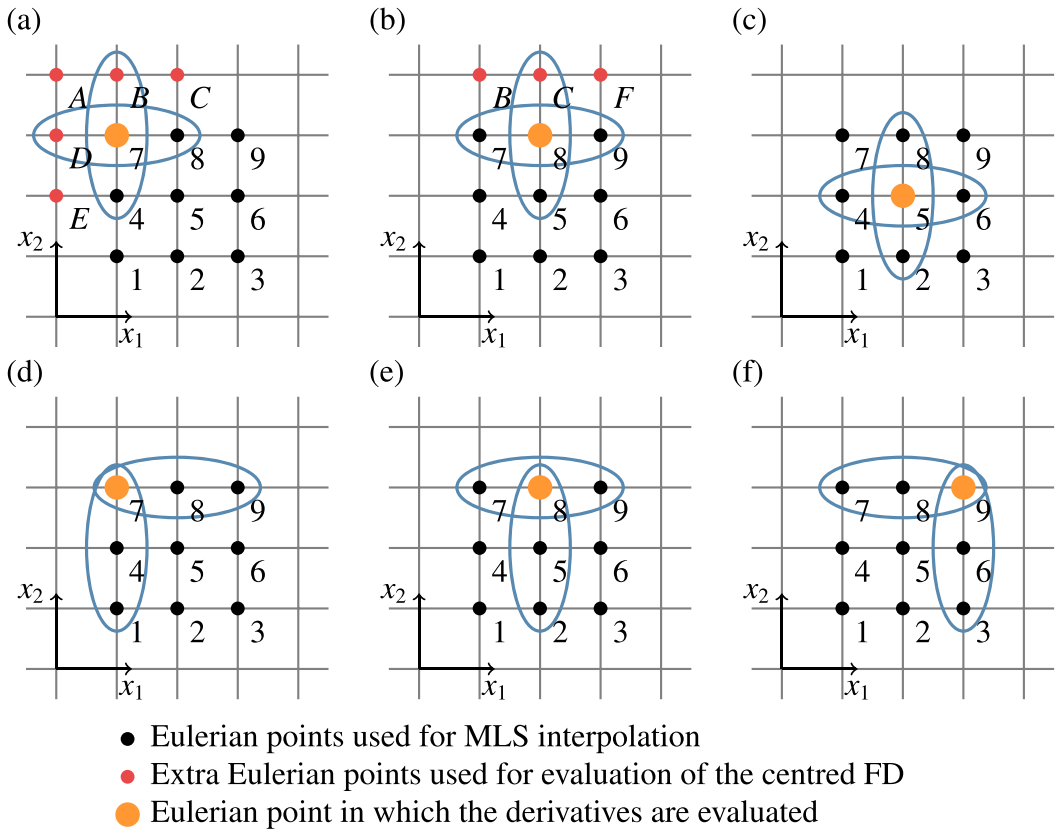


**Fig. B.1.** 2D sketch of the points required to evaluate the derivative of pressure and velocity on the MLS supporting domain points using the centred approach in points (a) 7, (b) 8 and (c) 5, and the off-centred approach in points (d) 7, (e) 8 and (f) 9. The FD stencil for the derivatives in $x_1$ and $x_2$ is highlighted in blue, while the stencil for the mixed derivative is omitted. (For interpretation of the references to colour in this figure legend, the reader is referred to the web version of this article.)

In the centred approach (see Fig. B.1a), the Eulerian derivatives are evaluated using a centred FD approximation on each point of the supporting domain. For instance, in the corner point 7 the first derivative of a scalar field $\phi$ (which could correspond either to pressure or to a velocity component) is given by:

$$\left.\frac{\partial \phi}{\partial x_1}\right|_7 = \frac{\phi_8 - \phi_D}{2\Delta} + \mathcal{O}(\Delta^2), \quad \left.\frac{\partial \phi}{\partial x_2}\right|_7 = \frac{\phi_B - \phi_4}{2\Delta} + \mathcal{O}(\Delta^2), \tag{B.1}$$

while the second derivatives are given by:

$$\left.\frac{\partial^2 \phi}{\partial x_1^2}\right|_7 = \frac{\phi_8 - 2\phi_7 + \phi_D}{\Delta^2} + \mathcal{O}(\Delta^2), \quad \left.\frac{\partial^2 \phi}{\partial x_2^2}\right|_7 = \frac{\phi_B - 2\phi_7 + \phi_4}{\Delta^2} + \mathcal{O}(\Delta^2), \tag{B.2}$$

and the mixed derivative:

$$\left.\frac{\partial^2 \phi}{\partial x_1 \partial x_2}\right|_7 = \frac{(\phi_C - \phi_A) - (\phi_5 - \phi_E)}{4\Delta^2} + \mathcal{O}(\Delta^2). \tag{B.3}$$

The points $A, B, C, D$ and $E$, required to evaluate the derivatives on point 7 with a centred scheme, are located outside the supporting domain of interpolation, thus enlarging the supporting domain needed to evaluate the traction. The same centred schemes can be used to evaluate the derivatives of $\phi$ at the side point 8, see Fig. B.1b. In this case, only the $x_2$ derivatives require an extra point, i.e. $C$, while the stencil for the $x_1$ derivatives is entirely contained within the MLS supporting domain of interpolation. For the mixed derivative, instead, the extra points $B$ and $F$ are required. As a final example for the centred approach, the FD stencil for the evaluation of the gradient of $\phi$ at the central point of the supporting domain is shown in Fig. B.1c, where the stencil of the FD is within the supporting domain of interpolation. The same scheme is applied to the other points (from 1 to 6), with the FD at the corner and edge points requiring additional points (with respect the interpolation supporting domain) to evaluate the coefficients of the Taylor series.

On the other hand, in the off-centred approach an upwind FD scheme is used, such that only the Eulerian points within the MLS-interpolation supporting domain are used. For instance, the off-centred FD scheme of the $x_1$ derivative of $\phi$ on point 7 is a forward

FD scheme, while for the $x_2$ derivative a backward scheme is employed (see Fig. B.1d):

$$\left.\frac{\partial\phi}{\partial x_1}\right|_7 = \frac{-\phi_9 + 4\phi_8 - 3\phi_7}{2\Delta} + \mathcal{O}(\Delta^2), \quad \left.\frac{\partial\phi}{\partial x_2}\right|_7 = \frac{3\phi_7 - 4\phi_4 + \phi_1}{2\Delta} + \mathcal{O}(\Delta^2). \tag{B.4}$$

For the second derivative, since only three stencil points per spatial direction are available, the following first order schemes (forward in $x_1$ and backward in $x_2$) are considered:

$$\left.\frac{\partial^2\phi}{\partial x_1^2}\right|_7 = \frac{\phi_9 - 2\phi_8 + \phi_7}{\Delta^2} + \mathcal{O}(\Delta), \quad \left.\frac{\partial^2\phi}{\partial x_2^2}\right|_7 = \frac{\phi_7 - 2\phi_4 + \phi_1}{\Delta^2} + \mathcal{O}(\Delta). \tag{B.5}$$

Instead, for the mixed term $\partial^2\phi/\partial x_1\partial x_2$, the intermediate derivatives in $x_1$ are evaluated with a forward scheme, while the ones in $x_2$ with a backward scheme, leading to:

$$\left.\frac{\partial^2\phi}{\partial x_1\partial x_2}\right|_7 = \frac{-3\phi_9 + 12\phi_8 - 9\phi_7 + 4\phi_6 - 24\phi_5 + 12\phi_4 - \phi_3 + 4\phi_2 - 3\phi_1}{4\Delta^2} + \mathcal{O}(\Delta^2) \tag{B.6}$$

On the other hand, for point 8 the $x_1$ derivative of $\phi$ can be obtained with a centred FD approximation, allowing for a second order approximation, while in the direction of $x_2$ a first order backward scheme is employed, as shown in Fig. B.1e. Finally, the derivatives at point 9 (see Fig. B.1f) are handled similarly to point 7, but the forward FD scheme in $x_1$ is replaced by a backward FD scheme, while the scheme for the derivatives in $x_2$ remains unchanged. The same reasoning apply to points $1, \dots, 6$, properly choosing the centred/backward/forward FD scheme based on the position of the considered point and of the differentiation direction. Clearly, for the central point 5, the (second order) centred FD scheme can be used for any derivative.

These two approaches apply to the 3D case in a straightforward manner.

## References


[1] F. Auguste, J. Magnaudet, D. Fabre, Falling styles of disks, J. Fluid Mech. 719 (2013) 388-405.
[2] M.M. Rajamuni, M.C. Thompson, K. Hourigan, Transverse flow-Induced vibrations of a sphere, J. Fluid Mech. 837 (2018) 931-966.
[3] S. Olivieri, F. Viola, A. Mazzino, M.E. Rosti, Direct numerical simulation of flapping flags in grid-induced turbulence, Phys. Fluids 33 (8) (2021) 085116.
[4] Z.J. Wang, Dissectin insect flight, Annu. Rev. Fluid Mech. 37 (1) (2005) 183-210.
[5] C.S. Peskin, Flow patterns around heart valves: a numerical method, J. Comput. Phys. 10 (2) (1972) 252-271.
[6] F. Viola, G. Del Corso, R. De Paulis, R. Verzicco, GPU Accelerated digital twins of the human heart open new routes for cardiovascular research, Sci. Rep. 13 (1) (2023) 8230.
[7] E.H. Dowell, K.C. Hall, Modeling of fluid-structure interaction, Annu. Rev. Fluid Mech. 33 (33) (2001) 445-490.
[8] G. Hou, J. Wang, A. Layton, Numerical methods for fluid-structure interaction — a review, Commun. Comput. Phys. 12 (2) (2012) 337-377.
[9] A.K. Slone, K. Pericleous, C. Bailey, M. Cross, Dynamic fluid–structure interaction using finite volume unstructured mesh procedures, Comput. Struct. 80 (5) (2002) 371-390.
[10] W. Dettmer, D. Perić, A computational framework for fluid–structure interaction: finite element formulation and applications, Comput. Methods Appl. Mech. Eng. 195 (41) (2006) 5754-5779.
[11] M. Uhlmann, An immersed boundary method with direct forcing for the simulation of particulate flows, J. Comput. Phys. 209 (2) (2005) 448-476.
[12] M. Vanella, E. Balaras, A moving-least-squares reconstruction for embedded-boundary formulations, J. Comput. Phys. 228 (18) (2009) 6617-6628.
[13] B.E. Griffith, N.A. Patankar, Immersed methods for fluid–structure interaction, Annu. Rev. Fluid Mech. 52 (1) (2020) 421-448.
[14] R. Verzicco, Immersed boundary methods: historical perspective and future outlook, Annu. Rev. Fluid Mec.h 55 (1) (2023) 129-155.
[15] J. Kim, P. Moin, Application of a fractional-step method to incompressible Navier-Stokes equations, J. Comput. Phys. 59 (2) (1985) 308-323.
[16] X. Zhu, E. Phillips, V. Spandan, J. Donners, G. Ruetsch, J. Romero, R. Ostilla-Mónico, Y. Yang, D. Lohse, R. Verzicco, M. Fatica, R.J.A.M. Stevens, AFiD-GPU: a versatile Navier–Stokes solver for wall-bounded turbulent flows on GPU clusters, Comput. Phys. Commun. 229 (2018) 199-210.
[17] M.D. de Tullio, G. Pascazio, A moving-least-squares immersed boundary method for simulating the fluid–structure interaction of elastic bodies with arbitrary thickness, J. Comput. Phys. 325 (2016) 201-225.
[18] S. Wang, M. Vanella, E. Balaras, A hydrodynamic stress model for simulating turbulence/particle interactions with immersed boundary methods, J. Comput. Phys. 382 (2019) 240-263.
[19] F. Dalla Barba, M. Zaccariotto, U. Galvanetto, F. Picano, 3D fluid–structure interaction with fracturing: a new method with applications, Comput. Methods Appl. Mech. Eng. 398 (2022) 115210.
[20] K. Zhong, C.J. Howland, D. Lohse, R. Verzicco, A front-Tracking immersed-boundary framework for simulating lagrangian melting problems, J. Comput. Phys. 525 (2025) 113762.
[21] X. Jiang, W. Huang, C. Xu, L. Zhao, A flow-reconstruction based approach for the computation of hydrodynamic stresses on immersed body surface, J. Comput. Phys. 508 (2024)113025.
[22] F. De Vita, M.D. de Tullio, A two-probe approach for hydrodynamic load evaluation in immersed boundary methods, J. Comput. Phys. 545 (2026) 114486.
[23] E.P. van der Poel, R. Ostilla-Mónico, J. Donners, R. Verzicco, A pencil distributed finite difference code for strongly turbulent wall-bounded flows, Comput. Fluids 116 (2015) 10-16.
[24] R. Verzicco, P. Orlandi, A.H.M. Eisenga, G.J.F.V. Heijst, G.F. Carnevale, Dynamics of a vortex ring in a rotating fluid, J. Fluid Mech. 317 (1996) 215 - 239.
[25] G.-R. Liu, Y.T. Gu, An Introduction to Meshfree Methods and Their Programming, Springer, Dordrecht, Dordrecht, 2010.
[26] J. Yang, E. Balaras, An embedded-boundary formulation for large-eddy simulation of turbulent flows interacting with moving boundaries, J. Comput. Phy.s 215 (1) (2006) 12-40.
[27] P.G. Drazin, N. Riley, The Navier-Stokes Equations: a Classification of Flows and Exact Solutions, Cambridge University Press, 1 edition, 2006.
[28] F. Hecht, New development in freefem + +, J. Numer. Math. 20 (3–4) (2012) 251–265. https://freefem.org/ 51-265.
[29] P. Meliga, J.-M. Chomaz, D. Sipp, Unsteadiness in the wake of disks and spheres: instability, receptivity and control using direct and adjoint global stability analyses, J. Fluids Struct. 25 (4) (2009) 601-616.
[30] J. Magnaudet, M. Rivero, J. Fabre, Accelerated flows past a rigid sphere or a spherical bubble. part 1. steady straining flow, J. Fluid Mech. 284 (1995) 97-135.
[31] W. Zhou, M. Chrust, J. Dusek, Path instabilities of oblate spheroids, J. Fluid Mech. 833 (2017) 445-468.
[32] M. Moriche, M. Uhlmann, J. Dusek, A single oblate spheroid settling in unbounded ambient fluid: a benchmark for simulations in steady and unsteady wake regimes, Int. J. Multiphase Flow 136 (2021) 103519.
[33] B. Wie (Ed.), Space Vehicle Dynamics and Control, AIAA Education Series, American Institute of Aeronautics and Astronautics, Reston, VA, 2nd ed edition, Reston, VA, 2008.

[34] W.-X. Huang, H.J. Sung, Three-dimensional simulation of a flapping flag in a uniform flow, J. Fluid Mech. 653 (2010) 301-336.
[35] F. Viola, G. Del Corso, R. Verzicco, High-fidelity model of the human heart: an immersed boundary implementation, Phys. Rev. Fluids 8 (10) (2023) 100502.
[36] N. Antonelli, R. Aristio, A. Gorgi, R. Zorrilla, R. Rossi, G. Scovazzi, R. Wüchner, The shifted boundary method in isogeometric analysis, Comput. Methods Appl. Mech. Eng. 430 (2024) 117228.